AGU PUBLICATIONS

JGR

Journal of Geophysical Research: Oceans

RESEARCH ARTICLE

10.1002/2015JC011112

Key Points:
- Air-sea gas exchange parameterizations methods are evaluated
- Schmidt number dependence on air-sea gas exchange
- Buoyancy dependence on air-sea gas exchange

Correspondence to:
S. T. Fredriksson,
sam.fredriksson@gu.se

Citation:
Fredriksson, S. T., L. Arneborg, H. Nilsson, Q. Zhang, and R. A. Handler (2016), An evaluation of gas transfer velocity parameterizations during natural convection using DNS, *J. Geophys. Res. Oceans*, *121*, 1400–1423, doi:10.1002/2015JC011112.

Received 8 JUL 2015
Accepted 18 JAN 2016
Accepted article online 25 JAN 2016
Published online 19 FEB 2016

Corrected 5 APR 2016
This article was corrected on 5 APR 2016. See the end of the full text for details.

An evaluation of gas transfer velocity parameterizations during natural convection using DNS

Sam T. Fredriksson[1], Lars Arneborg[1], Håkan Nilsson[2], Qi Zhang[3], and Robert A. Handler[3]

[1]Department of Marine Sciences, University of Gothenburg, Gothenburg, Sweden, [2]Department of Applied Mechanics, Fluid Dynamics, Chalmers University of Technology, Gothenburg, Sweden, [3]Department of Mechanical Engineering, Texas A&M University, College Station, Texas, USA

Abstract Direct numerical simulations (DNS) of free surface flows driven by natural convection are used to evaluate different methods of estimating air-water gas exchange at no-wind conditions. These methods estimate the transfer velocity as a function of either the horizontal flow divergence at the surface, the turbulent kinetic energy dissipation beneath the surface, the heat flux through the surface, or the wind speed above the surface. The gas transfer is modeled via a passive scalar. The Schmidt number dependence is studied for Schmidt numbers of 7, 150 and 600. The methods using divergence, dissipation and heat flux estimate the transfer velocity well for a range of varying surface heat flux values, and domain depths. The two evaluated empirical methods using wind (in the limit of no wind) give reasonable estimates of the transfer velocity, depending however on the surface heat flux and surfactant saturation. The transfer velocity is shown to be well represented by the expression, $k_s = A\ (B\nu)^{1/4}\ Sc^{-n}$, where A is a constant, B is the buoyancy flux, ν is the kinematic viscosity, Sc is the Schmidt number, and the exponent n depends on the water surface characteristics. The results suggest that $A = 0.39$ and $n \approx 1/2$ and $n \approx 2/3$ for slip and no-slip boundary conditions at the surface, respectively. It is further shown that slip and no-slip boundary conditions predict the heat transfer velocity corresponding to the limits of clean and highly surfactant contaminated surfaces, respectively.

1. Introduction

Recent global-model estimates suggest that inland waters (rivers, streams and lakes) are considerable sources of atmospheric greenhouse gases emitting as much as 1 Pg C yr^{-1} [*Bastviken et al.*, 2011; *Ciais et al.*, 2013; *Tranvik et al.*, 2009]. Furthermore, these emissions are of the same magnitude as the ocean net sink that is estimated to be 1.6 Pg C yr^{-1} [*Ciais et al.*, 2013]. It has also been shown that the ocean global mean heat flux is increasing [*Pierce et al.*, 2006; *Yu and Weller*, 2007]. The ocean heat flux is an important driver for the atmosphere circulation and the coupled ocean-atmosphere. The ability to model heat and gas flux is therefore critical for predictions of the global climate. The gas flux is the main focus in the present study although the results have implications also for the heat transfer velocity. Most available estimates of CO_2 and diffusive CH_4 emissions from aquatic ecosystems rely on empirical functions of the gas transfer velocity

$$k_g = F/(c_w - \vartheta c_a). \tag{1}$$

Here F is the gas flux, ϑ is the Ostwald solubility coefficient of the gas in water, and c_w and c_a are the gas concentrations in the surface water under the diffusive sublayer (bulk) and in the air respectively. k_g is often parameterized as a function of the wind speed U_{10} defined as the wind speed 10 m above the water surface. However, the wind speed parameterizations of k_g show large discrepancies for low wind conditions and some models even estimate k_g to be zero for no-wind conditions [*Donelan and Wanninkhof*, 2002]. This is primarily because other sources of turbulence near the surface, e.g., buoyancy forcing and rain, are not included in these parameterizations. The relevance for studying low-wind conditions can i.e., be seen in the work of *Jonsson et al.* [2008] and *Vesala et al.* [2006] where they compare the eddy covariance method with the wind parameterization method by *Cole and Caraco* [1998] during several months for two typical small lakes in Sweden and Finland. *Jonsson et al.* [2008] record a mean U_{10} of 3.9 ms^{-1} and *Vesala et al.* [2006] only occasionally recorded U_{10} above 2 ms^{-1} for the more than 200 days long measurement period. *Cole*

et al. [2007] finally conclude that "There is little doubt that the neutral pipe hypothesis [for freshwater] is untenable, and that freshwater ecosystems represent an active component of the global carbon cycle that deserve attention."

There are parameterizations that do include both the wind via the friction velocity, and the influence of buoyancy flux and mixed layer depth via a convective velocity scale in a surface renewal model [*Macintyre et al*., 2002], a resistance model [*Rutgersson et al*., 2011] or an additional ocean gustiness model [*Jeffery et al*., 2007]. However, there is a general lack of consistency between these different approaches and it is not yet certain to what extent these processes affect the transfer velocity for different flow conditions. In addition to the wind speed parameterizations, there are a number of methods that parameterize the gas transfer velocity in terms of parameters more directly related to the surface conditions, and the subsurface turbulence. Examples of methods in use are infrared imaging of the surface temperature [*Asher et al*., 2012; *Gålfalk et al*., 2013; *Handler and Zhang*, 2013; *Veron et al*., 2008; *Zappa et al*., 2003, 2004], turbulent kinetic energy dissipation measurements below the surface [*Jessup et al*., 2009; *Lamont and Scott*, 1970; *Zappa et al*., 2007], and horizontal flow divergence measurements at the water surface [*Asher et al*., 2012; *McKenna and McGillis*, 2004].

Direct numerical simulations (DNS) and large eddy simulations (LES) have been used with success to study air-sea gas exchange as a function of the horizontal flow divergence [*Banerjee et al*., 2004; *Calmet and Magnaudet*, 1998; *Magnaudet and Calmet*, 2006] or its dependence on turbulent kinetic energy dissipation via a turbulent Reynolds number Re_T [*Calmet and Magnaudet*, 1998]. In addition, simulations have been used to study how the gas transfer velocity depends on the Schmidt number [*Hasegawa and Kasagi*, 2008; *Herlina and Wissink*, 2014; *Na et al*., 1999; *Nagaosa and Handler*, 2012; *Nagaosa*, 2014]. *Kubrak et al*. [2013] have used a refined dual mesh technique in order to obtain negligible numerical diffusion for two-dimensional simulations of scalars with high *Sc*. DNS has also been used to investigate the influence of surfactants on the gas exchange [*Hasegawa and Kasagi*, 2008; *Zhang et al*., 2013].

The main objective of the present work is to study and evaluate different gas transfer velocity parameterization methods. These include two standard wind parameterizations (in the limit of no wind), as well as parameterizations in terms of heat flux, horizontal flow divergence, and turbulent kinetic energy dissipation. The flow under consideration is driven by natural convection only, which is a situation relevant to small sheltered lakes as well as for low wind conditions in the ocean and larger lakes. The evaluation is performed using DNS. The surface heat flux, the domain depth, and the Schmidt number are altered in parameter analyses. This is, to the best knowledge of the authors, the first time these gas transfer velocity parameterizations have been evaluated altogether in a highly resolved numerical study for flows driven by natural convection, enabling a systematic and consistent comparison of the parameterizations.

1.1. Gas Transfer Parameterizations

The factors affecting the gas exchange across an air-water interface can be divided into biochemical and physical ones. Biochemical factors, not considered in this study, are typically chemical or biological processes that produce or consume gas. Physical factors include e.g., advective and diffusive transports. The actual gas exchange is, when bubbles or raindrops are not present, maintained by molecular diffusion across the air-water interface, and for slightly soluble gases, e.g., CO_2 and CH_4, this diffusive gas exchange is limited by the aqueous phase [*Bade*, 2009]. This allows studies of the exchange dynamics to be performed in the aqueous phase only, with boundary conditions imposed from the air side. For the water side, the advective motions dominate the transport of gas from the deeper water masses up to the diffusive sublayer, in which the vertical motions are attenuated and the molecular diffusion eventually takes overs. The gas transfer velocity, k_g, given in equation (1) is then used to estimate the gas flux across the air-water interface.

It is common to estimate the k_g by using the wind speed 10 meters above the surface, referred to as U_{10}. The present study supposes that the flow is driven by natural convection only, and the evaluations are therefore limited to the no-wind condition limit of the wind speed parameterizations. The two evaluated parameterizations with nonzero gas transfer velocities for the no-wind conditions are given by *Cole and Caraco* [1998] as

$$k_{g,CC1998,600} = 0.215U_{10}^{1.7} + 2.07 \quad (2)$$

often used for inland waters and *Wanninkhof et al.* [2009] as

$$k_{g,W2009,660} = 0.1U_{10} + 0.064U_{10}^{2} + 0.011U_{10}^{3} + 3 \quad (3)$$

often used for ocean conditions. These empirical equations have nonzero transfer velocities even for $U_{10}=0$ which may be explained by other transfer enhancing processes than wind (e.g., convection) that affect the transfer. Further, it can be seen that equations (2) and (3) are dimensionally inconsistent and it is therefore necessary to use the correct units in order to get the correct transfer velocities. The wind speed, U_{10}, is given in units of (m s^{-1}) whereas the transfer velocities are given in (cm h^{-1}). Equations (2) and (3) are given for a gas with Schmidt number $Sc=600$ and $Sc=660$, respectively, where $Sc=\nu/D$, ν is the kinematic viscosity, and D is the molecular diffusion coefficient. Gas transfer velocities for different gases are then generally converted as

$$\frac{k_{g,1}}{k_{g,2}} = \left(\frac{Sc_1}{Sc_2}\right)^{-n} \quad (4)$$

where $1/2 < n < 2/3$ dependent of the water surface characteristics [*Bade*, 2009; *Wanninkhof et al*., 2009].

More direct methods parametrize the gas exchange velocity in terms of the dissipation of turbulent kinetic energy, surface divergence, and heat flux velocity. The theoretical framework for the parameterization method using the turbulent kinetic energy dissipation [*Banerjee et al*., 1968; *Lamont and Scott*, 1970] is a continuation of the eddy cell model [*Fortescue and Pearson*, 1967], but with the assumption that it is the small-scale dissipative eddies that are the main transportation agents. This assumption, together with a standard turbulence spectrum, yields the transfer velocity as

$$k_{g,diss} = A_{diss}(\varepsilon\nu)^{1/4}Sc^{-n}. \quad (5)$$

Here A_{diss} is a transfer velocity constant, ε is the rate of turbulent kinetic energy dissipation, and $n=1/2$ $(2/3)$ for a free fluid (solid) surface respectively [*Lamont and Scott*, 1970]. Although none of the assumptions are strictly fulfilled in reality, this model has proven to give reasonable results in many cases [*Gålfalk et al*., 2013; *Zappa et al*., 2007].

The horizontal flow divergence at the surface, $\gamma=\partial u/\partial x+\partial v/\partial y$, has been used as a proxy for the gas transfer velocity in many studies [*Banerjee et al*., 2004; *Calmet and Magnaudet*, 1998; *McKenna and McGillis*, 2004]. Here u and v are the horizontal velocities in the x and the y direction, see Figure 1. The gas transfer velocity is expressed as

$$k_{g,div} = A_{div}(\gamma_{rms}\nu)^{1/2}Sc^{-n}, \quad (6)$$

where A_{div} is a transfer velocity constant. Both the mean and the root-mean-square (rms) of the surface flow divergence have previously been used, but in the present work we use the rms, γ_{rms}. *McKenna and McGillis* [2004] suggest $1/2 < n < 2/3$ depending on the amount of surfactants on the water surface.

The surface heat flux, Q, and the heat transfer velocity, κ_{heat}, have been used [*Frew et al*., 2004; *Jahne and Haussecker*, 1998] to estimate the gas transfer velocity as

$$k_{g,heat} = A_{heat}\kappa_{heat}\left[\frac{Sc}{Pr}\right]^{-n}, \quad \kappa_{heat} = \frac{Q}{\rho c_p \Delta T} \quad (7)$$

where $Pr=\nu/\alpha$ is the Prandtl number, α is thermal diffusivity, and A_{heat} is a transfer velocity constant. In addition ΔT is the surface-skin to bulk temperature difference here defined as the temperature difference between the top of the domain (the surface) and at the depth where the vertical gradient of the temperature becomes zero, ρ is the density, and c_p is the specific heat capacity. This expression is based on the assumption that heat transfer is analogous to gas transfer. The three main differences between heat and gas transfer are: (i) That heat influences the buoyancy, (ii) That the surface boundary conditions for gas and heat are different, and (iii) That the diffusivities can be orders of magnitude different with $Pr=\mathcal{O}(10^0)$ and $Sc=\mathcal{O}(10^2)$ depending on which gas it is. In spite of these differences, e.g., *Jahne et al*. [1989] have shown that there is a good agreement between directly measured oxygen ($Sc=\mathcal{O}(10^2)$) transfer velocities and

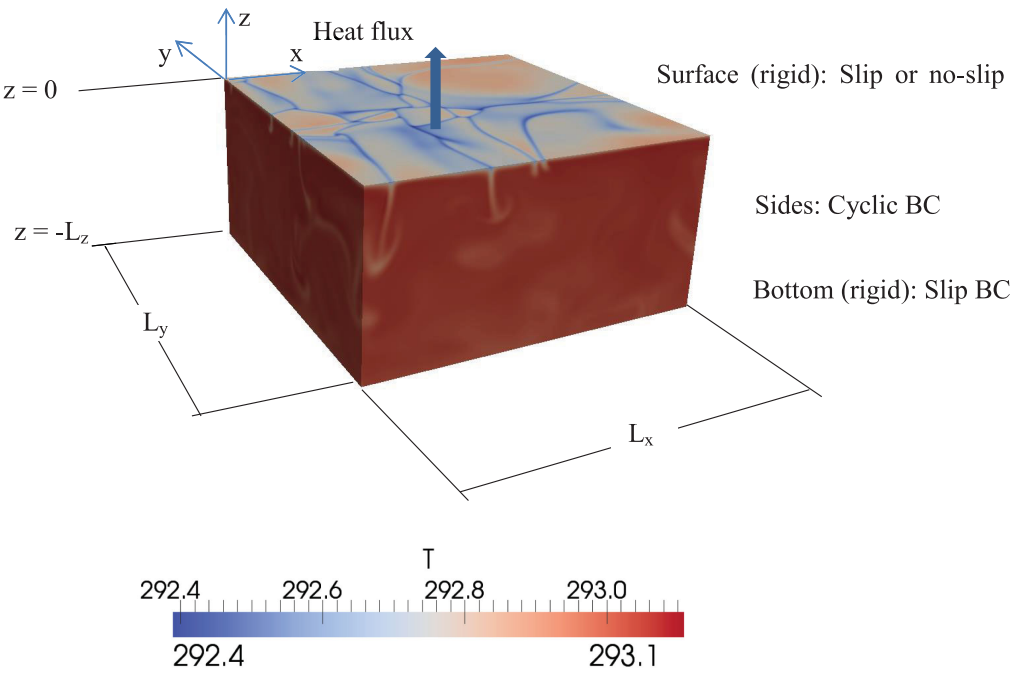

Figure 1. Computational domain. The surface heat flux cools the water and forms thin descending plumes of denser cold water.

extrapolated transfer velocities from the heat transfer velocity. To our knowledge nobody has quantified the importance of each of these differences, as we will do here.

1.2. Scaling

The use of nondimensional numbers and scaling of our problem aid significantly in understanding which processes and scales that are important in determining the transfer velocity. The nondimensional numbers normally used to understand and describe the physics of flows driven by natural convection are *Pr*, *Sc*, and the Rayleigh number,

$$Ra = \frac{\beta g Q L^4}{\alpha \upsilon \lambda} = \frac{B L^4}{\alpha^2 \nu}, \tag{8}$$

where β is the coefficient of thermal expansion, g is the gravitational acceleration, α is the thermal diffusivity, $\lambda = \rho c_p \alpha$ is the thermal conductivity, and *L* is a characteristic length. *B* is the buoyancy flux defined as

$$B = \frac{\beta g Q}{\rho c_p}. \tag{9}$$

Three standard scaling schemes for turbulent scaling were presented by *Adrian et al.* [1986] as: (i) inner scaling originating from *Townsend* [1959], (ii) outer scaling originating from *Deardorf* [1970], and (iii) Rayleigh scaling. The inner and outer scaling (see Table 1) are denoted by $(\cdot^+)$ and $(\cdot^*)$. Rayleigh scaling is appropriate for the analysis of the stability of natural convection but it is not suited for the scaling of mass transport which is the subject for the present work. However, for completeness, *Ra* numbers are given in the summary of the numerical cases in Table 2. The inner scaling used in the present work is based on the surface strain model of *Csanady* [1990], and can be used for a wide variety of situations where e.g., shear and wave

Table 1. Scaling Schemes

Scheme	Length	Velocity	Time	Temperature	Scalar	Flow Divergence
Inner	$L^+ = Sc^{n-1}\left(\frac{\nu^3}{B}\right)^{1/4}$	$W^+ = Sc^{-n}(B\nu)^{1/4}$	$t^+ = Sc^{2n-1}\left(\frac{B}{\nu}\right)^{-1/2}$	$\theta^+ = Q_0 Pr^n (B\nu)^{-1/4}$	$s^+ = F_s Sc^n (B\nu)^{-1/4}$	$\gamma^+ = 1/t^+$
Outer[a]	$L^* = L_z$	$W^* = (BL^*)^{1/3}$	$t^* = \left(\frac{B}{L^{*2}}\right)^{-1/3}$	$\theta^* = Q_0 (BL^*)^{-1/3}$	$s^* = F_s (BL^*)^{-1/3}$	$\gamma^* = 1/t^*$

[a]The mixing layer depth in these simulations is assumed to be the domain depth L_z.

Table 2. Summary of Numerical Cases

Case[a]	BC	L_x, L_y	L_z[b]	Q[c]	Ra	Sc	Resolution[d]	Δz[e]
s2B	**slip**	$\mathbf{2L_z}$	$\boldsymbol{L_{z,B}}$	$\boldsymbol{Q_B}$	5.0×10^8	**7,150,600**	**256**×256×**96**	**1.96/0.098**
s2C	slip	$2L_z$	$L_{z,B}$	Q_B	5.0×10^8	-	128×128×96	1.96/0.098
s2F	slip	$2L_z$	$L_{z,B}$	Q_B	5.0×10^8	7,150,600	402×402×96	1.96/0.098
s1B	slip	L_z	$L_{z,B}$	Q_B	5.0×10^8	-	128×128×96	1.96/0.098
sπB	slip	πL_z	$L_{z,B}$	Q_B	5.0×10^8	-	402×402×96	1.96/0.098
s2BL	slip	$2L_z$	$L_{z,B}$	$Q_B/2$	2.5×10^8	7	256×256×96	1.96/0.098
s2BH	slip	$2L_z$	$L_{z,B}$	$2Q_B$	10×10^8	7	256×256×96	1.96/0.098
s2BS	slip	$2L_z$	$2L_{z,B}/\pi$	Q_B	0.8×10^8	7	163×163×106	0.47/0.098
s2BD	slip	$2L_z$	$\pi L_{z,B}/2$	Q_B	30×10^8	7	402×402×226	0.47/0.098
n2B	no-slip	$2L_z$	$L_{z,B}$	Q_B	5.0×10^8	7,150,600	256×256×96	1.96/0.098

[a] *s* and *n* denote Slip and No-slip boundary conditions. *1*, *2* and *π* denote the ratio between horizontal domain size, L_x, and domain depth, L_z . *C*, *B* and *F* denote Coarse, Base and Fine horizontal mesh respectively. *L* and *H* denote Low and High heat flux. *S* and *D* denote Shallow and Deep domain.
[b] $L_{z,B}=0.1204$ *m*.
[c] $Q_B=100$ Wm^{-2}.
[d] In x, y and z directions.
[e] Distance from bottom and surface boundaries to the center of the first cells, respectively (mm).

breaking are important in addition to buoyancy. *Leighton et al*. [2003] developed the surface-strain model further, for a natural convection driven case with a slip boundary condition, by linking the surface strain to the turbulent energy dissipation, buoyancy and heat flux. The link is achieved by assuming that $\varepsilon \sim \upsilon\gamma^2$ and that the dissipation scales with the turbulence production, which in the present case can be scaled with the buoyancy flux, i.e., $\varepsilon \sim B$. In the present work we extend this latter scaling to be valid also for a no-slip surface boundary condition. For an inner length scale L^+ representing the thickness of the diffusive sublayer, the inner velocity scale W^+ and the gas transfer velocity scales as

$$W^+ = \frac{D}{L^+} \sim k_g \tag{10}$$

where D is the molecular diffusion coefficient. By using the eddy-cell and the strain models and leaving out the constants that appear in these models the following length, velocity, and scalar concentration scaling are obtained

$$L^+ = Sc^{n-1}\left(\frac{\nu^3}{B}\right)^{1/4} \left(\sim Sc^{n-1}\left(\frac{\nu^3}{\varepsilon}\right)^{1/4} = Sc^{n-1}L_K\right) \tag{11}$$

$$W^+ = Sc^{-n}(B\nu)^{1/4} \left(\sim Sc^{-n}(\varepsilon\nu)^{1/4}\right) \tag{12}$$

$$s^+ = \frac{F_s}{W^+} = F_s Sc^n (B\nu)^{-1/4} \left(\sim F_s Sc^n (\varepsilon\nu)^{-1/4}\right) \tag{13}$$

where L_K is the Kolmogorov length scale [*Kundu et al*., 2012]. In order to obtain a heat flux scaling, Sc is replaced by Pr, F_s is replaced by the kinematic heat flux $Q_0=Q/\rho c_p$, and s^+ is replaced by θ^+. The resulting scaling is consistent with *Csanady* [1990] and *Leighton et al*. [2003] for the slip case ($n = 1/2$) except for some constants (i.e., $L_{sm}=\sqrt{2}L^+$ and $s_{sm}=\sqrt{\pi/2}s^+$) that we avoid for the sake of simplicity. L^+ is also seen to be proportional to the Batchelor length scale L_B [*Kundu et al*., 2012] for $n = 1/2$.

The outer scales are defined as

$$L^* = L_z, \quad W^* = (BL^*)^{1/3}, \quad \theta^* = \frac{Q_0}{W^*}, \quad s^* = \frac{F_s}{W^*} \tag{14}$$

The scales for the turbulent heat and scalar transport are then $W^+s^+=F_s$, $W^+\theta^+=Q_0$, $W^*s^*=F_s$ and $W^*\theta^*=Q_0$, i.e., the same for inner and outer scaling respectively.

2. Problem Formulation and Numerical Methods

The transport of a dissolved gas is modeled using a passive scalar in DNS of fully developed turbulent natural convective flow. The computational domain, shown in Figure 1, is supposed to represent the surface

layer of the oceans or lakes, meaning that the lateral dimensions are large enough that the results represent those for an infinite surface, and the vertical dimension is large enough that the results are representative for the surface mixed-layer of the oceans or lakes. The results in the present study support this assumption even though the dimensions of the computational domain are much smaller than in reality. The surface is located at $z = 0$ and the bottom boundary at $z = -L_z$. The lateral dimensions are given by L_x and L_y respectively. A summary of the simulations is given in Table 2. The simulations are labeled with a letter describing the velocity boundary condition at the surface, a number describing the domain width to depth ratio, and a letter describing the horizontal mesh resolution. The labels for the simulations with varying surface heat flux or domain depth use a fourth letter (L and H for low and high heat flux and S and D for shallow and deep domain respectively). The scalar flux F_s across the air-water interface and in turn the scalar transfer velocity

$$k_{s,Sc} = \frac{F_{s,Sc}}{\Delta S_{Sc}} \tag{15}$$

is used as a measure to study the parameterizations of the gas transfer velocity. Here $F_{s,Sc}$ is the scalar flux across the surface for a scalar with a Schmidt number Sc and ΔS_{Sc} is the scalar-concentration difference between the top of the domain (the surface) and at the depth where the vertical gradient of the concentration becomes zero. The gas-transfer velocity parameterizations of $k_g = k_g\left(\varepsilon, \gamma, Q/\Delta T, \nu, c_p, Sc, n, U_{10}\right)$ in equations (2–7) are studied by evaluating $\varepsilon, \gamma, Q/\Delta T$, and estimating n while varying Sc, the surface heat flux, and the domain depth. ν, c_p, and U_{10} and remain fixed in all cases.

2.1. Numerical Methods

The equations for solving a flow driven by natural convection [*Leighton et al.*, 2003] are here presented together with the equations to be solved for the scalar concentration. The standard Boussinesq approximation is used, in which density variations are assumed to be sufficiently small to have a negligible effect on the inertial terms in the momentum equation, and act only to generate buoyancy forces. The density ρ is assumed to be a linear function of the temperature T as

$$\rho(T) = \rho_0 \ (1 - \beta(T - T_0)), \tag{16}$$

where $\beta = -\frac{1}{\rho_0} \ \frac{\partial \rho}{\partial T}|_0$ is the coefficient of thermal expansion, ρ_0 is the reference density, and T_0 is a reference temperature. Under the Boussinesq approximation the Navier-Stokes equations can be written as:

$$\frac{\partial \mathbf{U}}{\partial t} + \mathrm{U} \cdot \nabla \mathbf{U} = -\frac{1}{\rho_0} \nabla P + \nu \nabla^2 \mathbf{U} + \beta \ (T - T_0)\mathbf{g} \tag{17}$$

$$\nabla \cdot \mathbf{U} = 0 \tag{18}$$

Here $\mathbf{U} = (U, V, W)$ is the fluid velocity whose components are given in the x, y, z coordinate directions respectively, t is time, P is a modified pressure with the background hydrostatic pressure for a constant density subtracted, ν is the kinematic viscosity, and $\mathbf{g}$ is the gravitational acceleration. The temperature development is determined by the thermal energy equation

$$\frac{\partial T}{\partial t} + \mathbf{U} \cdot \nabla T = \ \alpha \nabla^2 T + \phi_T, \tag{19}$$

where ϕ_T is a spatially and temporally constant source term added to maintain a constant mean temperature.

The surface (top boundary) is modeled as a flat surface under the assumption that the surface deflection is negligible. The velocity boundary conditions are set to either a slip condition using

$$\frac{\partial U}{\partial z} = \frac{\partial V}{\partial z} = 0, \ W = 0, \tag{20}$$

or a no-slip condition using

$$U = V = W = 0. \tag{21}$$

The bottom boundary is assumed to be stress-free and is thus given a slip boundary condition. During natural-convection conditions with no wind, the surface heat flux is dominated by long-wave radiation and

latent heat flux, both of which we assume to be constant in these simulations. The top boundary condition for the temperature is thus set to

$$\frac{\partial T}{\partial z} = -\frac{Q}{\lambda} \quad \text{at } z=0\,, \tag{22}$$

where $Q>0$ is a constant flux directed out of the surface boundary [*Soloviev and Schlussel*, 1994]. The bottom is assumed to be insulated (no heat exchange with lower water masses) and thus the bottom boundary condition is given by:

$$\frac{\partial T}{\partial z} = 0. \tag{23}$$

The dissolved gas is modeled as a passive scalar concentration S via:

$$\frac{\partial S}{\partial t} + \mathbf{U} \cdot \nabla S = D\nabla^2 S + \phi_s \tag{24}$$

where $\phi_s = F_s/L_z$ is a spatially evenly distributed and temporally constant source term and F_s is the flux through the surface. For the passive scalar we use the boundary conditions:

$$S = S_0 \tag{25}$$

and

$$\frac{\partial S}{\partial z} = 0 \tag{26}$$

for the top and bottom boundaries respectively. Here S_0 is the constant scalar concentration at the surface. The assumption of a constant concentration at the surface is derived from the fact that the horizontal concentration gradients at the air-water interface are assumed to be much smaller in the air than in the water depending on the gas-water solubility.

Finally, the flow is subject to periodic boundary conditions in the horizontal (x and y) directions. $\mathbf{u} = (u, v, w)$, θ, and s are the fluctuating parts of the velocity, temperature, and scalar concentration respectively.

2.1.1. Solver and Discretization

The simulations are carried out using OpenFOAM. This parallel computational fluid dynamics tool and its collocated finite volume approach were chosen in order to eventually increase the complexity of our study with wind shear stress, followed by ripples and wind waves. Another advantage of OpenFOAM is that it is open source and therefore easily accessible for reproducibility, as well as for further research and development. The time derivative is discretized using the second-order Crank-Nicolson scheme and the diffusion and advection terms are discretized using the second-order central differencing scheme [*Versteeg and Malalasekera*, 2007]. The PIMPLE algorithm of OpenFOAM is used with eight outer corrector steps and one corrector step for each time step.

The time step, Δt, is chosen in order to comply with criteria for both the Kolmogorov time scale $t_K = (\nu/\varepsilon)^{1/2}$ [*Kundu et al*., 2012] and the Courant-Friedrichs-Lewy (CFL) number

$$\mathrm{CFL} = \frac{\Delta t |\mathrm{U}|}{\Delta l}. \tag{27}$$

Here $|\mathrm{U}|$ is the magnitude of the velocity through a cell with a length, Δl, in the direction of the velocity. The time step Δt is dynamically adjusted to keep $\mathrm{CFL} < 0.5$ in all cells which typically gives a time step much smaller than the Kolmogorov time scale, and is therefore the limiting time step constraint. The space discretization (mesh resolution) is discussed in section 3.1.1.

2.1.2. Sampling Time

The sampling of the results is done under fully developed conditions, defined by steady mean and root-mean-square (rms) for all the variables. Mean and rms values are obtained by a combination of ensemble averaging and averaging over horizontal planes. The sampling is carried out for more than 40 large eddy time scales, t^*, defined as

$$t^* = \frac{L_z}{W^*}. \tag{28}$$

This corresponds to more than 500 t^+ where the inner time scale t^+ is given by

$$t^+ = \frac{L^+}{W^+} = \left(\frac{\rho c_p \nu}{\beta g Q}\right)^{1/2}. \quad (29)$$

3. Results and Discussion

Section 3.1 presents a numerical sensitivity study where the sensitivity of rms velocity and temperature, mean temperature and horizontal flow divergence, and rate of turbulent kinetic energy dissipation, to the mesh resolution and to the domain width to depth aspect ratio is analyzed. Section 3.2 presents the results from the cases with varying surface velocity-boundary-conditions where the results for the slip and the no-slip boundary conditions are compared to those in the pseudo-spectral code study by *Zhang et al*. [2013], hereinafter referred to as ZHF, with a surfactant surface velocity-boundary-condition. Section 3.3 presents a parameter study of the different surface boundary conditions for the temperature and the scalar. This is followed by section 3.4 where a parameter study for the domain depth and surface heat flux is presented. The different parameterizations of the gas transfer velocity are evaluated in section 3.5, and section 3.6 presents the results from the Schmidt-number parameter-study. The results and discussion section is closed by section 3.7 where a new expression for the mass transfer velocities under natural convective forcing is presented.

3.1. Sensitivity to Mesh Resolution and Domain Aspect-Ratio

This section focuses on the sensitivity of the Navier-Stokes and thermal energy equations (17–19) to the computational mesh, while the sensitivity of the scalar transport equation to the mesh resolution is discussed in section 3.6. The domain depth and the surface heat flux are constant during both the mesh and the domain aspect ratio sensitivity study. The mesh resolution study is performed using a constant domain size, while the domain aspect-ratio sensitivity study is performed using a constant cell size. The results are compared to those for the *Clean* case (without surfactant) from ZHF which can be considered as a slip (shear free) surface boundary condition case.

3.1.1. Mesh Resolution Sensitivity

The case labels *s2C*, *s2B* and *s2F* stand for slip surface boundary condition for which $L_x = L_y = 2L_z$ with a Coarse, Base ($\Delta x \approx 0.5\ L_K \approx 1.3 L_B$) and Fine horizontal mesh resolution respectively. Δx is the horizontal mesh size. The Kolmogorov length scale,

$$L_K = \left(\frac{\nu^3}{\varepsilon}\right)^{1/4}, \quad (30)$$

where ε is assumed to equal B, and the Batchelor length scale for temperature,

$$L_B = Pr^{-1/2} L_K \left(= Sc^{-1/2} L_K\right), \quad (31)$$

were previously discussed in relation to the inner length scale defined in equation (11). The meshes are nonuniform in the vertical direction (i.e., finer resolution near the top boundary). The thinnest cell close to the top boundary is 20 times smaller than the cell closest to the bottom whereas the grid stretching in the *Clean* case in ZHF results in the same grading at the top and bottom of the domain. The high vertical mesh resolution ($\Delta z \approx 0.1\ \Delta x$) close to the surface is the reason for performing horizontal mesh resolution studies only. The vertical mesh resolution close to the bottom is discussed in the end of this section. Figure 2 shows a comparison between the normalized surface temperature field from *s2C* and *s2B* from present work and the *Clean* case from ZHF. All the temperature fields show similar scales of the structures at the surface. Unphysical oscillations are present in *s2C* but not in ZHF, although the horizontal resolution in *s2C* is the same as in ZHF. The oscillations decrease with the higher mesh resolution in *s2B* and vanish in *s2F* (not shown here). Figure 3 shows the rms velocity, the mean and rms temperature, the mean horizontal flow divergence, and the rate of turbulent kinetic energy dissipation:

$$\tilde{\varepsilon} = \nu \frac{\partial u_i \partial u_i}{\partial x_k \partial x_k} = \varepsilon - \nu \frac{\partial u_i \partial u_k}{\partial x_k \partial x_i} \quad (32)$$

Here ε is the true viscous dissipation, $\tilde{\varepsilon}$ is the so called pseudo-dissipation, and $\langle\ \rangle_i$ and $\langle\ \rangle_k$ denote the three velocity components and coordinate directions in Figure 1. The pseudo-dissipation is used in all the

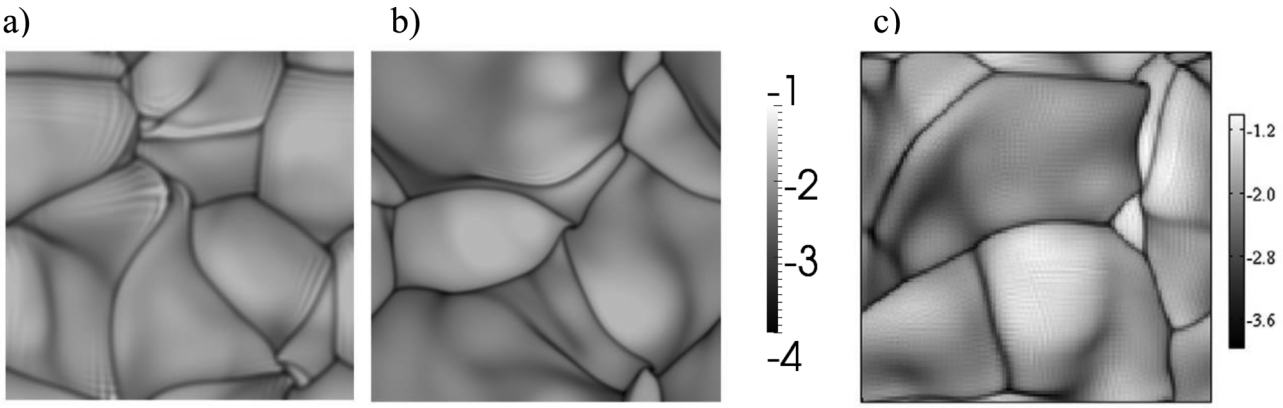

Figure 2. Surface temperature fields normalized with $\theta_{sm}=\theta^{+}\sqrt{\pi/2}$ defined in ZHF. (a) Present work with coarse mesh, *s2C*, and (b) base mesh, *s2B*, respectively. (c) *Clean* from ZHF.

plots and equation (5) since estimations of the rate of turbulent kinetic energy dissipation in field measurements [*Gålfalk et al*., 2013; *Zappa et al*., 2003, 2007] typically is the pseudo-dissipation. It is also the pseudo-dissipation that is used in the derivation of the inner scaling by *Leighton et al*. [2003]. The mesh dependence for ε and $\tilde{\varepsilon}$ is further discussed in section 3.5.2 where the transfer velocity as a function of $\tilde{\varepsilon}$ is presented. It can be seen in the insets of Figures 3a and 3b that the fluctuating vertical velocity, w_{rms}, and the fluctuating temperatures are relatively unaffected by the horizontal mesh resolution. Close to the surface there is a small mesh resolution dependency in the fluctuating horizontal velocity (variations $<\pm2\%$), the mean temperature (mean and ΔT variations $<\pm1.3\%$), the turbulent kinetic energy dissipation (variations $<\pm3.5\%$), and the mean horizontal flow divergence (variations $<\pm1\%$). The mesh influence on the horizontal fluctuating velocity is considered to be acceptable, since the main interest in this study is the vertical mass transfer where it is the fluctuating vertical velocity that plays the major role. The parameterizations of the mass transfer velocity as a function of: (i) The turbulent kinetic energy dissipation, $k_{g,diss}\propto\varepsilon^{1/4}$, (ii) The fluctuating horizontal flow divergence, $k_{g,div}\propto\gamma^{1/2}$, and (iii) The heat flux, $k_{g,heat}\propto\Delta T^{-1}$, in equations (5–7) result in a mesh resolution influence of approximately 1% which is also considered acceptable. This also implies that it is possible to use a coarser mesh, as in *s2C*, resulting in oscillations at the surface, without significantly influencing the flow statistics presented in Figure 3, or the gas transfer velocity parameterizations $k_{g,diss}$, $k_{g,div}$, and $k_{g,heat}$.

The viscous and thermal boundary layers are well resolved by approximately 20 cells and it is seen in Figures 3 and 4 by comparing the results from present study with the *Clean* case from ZHF that the different mesh grading close to the bottom boundary for the present study and the *Clean* case does not significantly influence the results at the top boundary.

3.1.2. Domain Aspect Ratio Sensitivity

For the base mesh resolution, *s2B*, the domain aspect ratio was studied in cases *s1B* and *sπB* as presented in Table 2 and Figure 3. Close to the surface there is a domain width dependency with a decreasing rms horizontal velocity for the aspect ratio of one, *s1B*. Besides that, the domain width dependencies are small for the horizontal rms velocity (variations $<\pm2\%$ for *s2B* and *sπB*), the mean temperature (variations $<\pm2\%$), the turbulent kinetic energy dissipation (variations $<\pm1.2\%$), and the mean horizontal flow divergence (variations $<\pm1\%$). The domain aspect ratio $L_x/L_z=L_y/L_z=2$ is therefore considered large enough for the present work.

3.2. Surface Velocity Boundary Conditions

Surface active chemical agents (surfactants) are almost always present in natural waters. Spatially and temporally varying surfactant concentration gradients generate corresponding surface tension gradients that attenuate the near-surface turbulence. This attenuation of the turbulence is studied via case *s2B* and *n2B* in present work and the cases in ZHF. The Marangoni number

$$Ma=-\left(\frac{d\bar{\sigma}}{d\bar{\psi}}\right)\Big|_0 \tag{33}$$

is often used to characterize a surfactant. Here

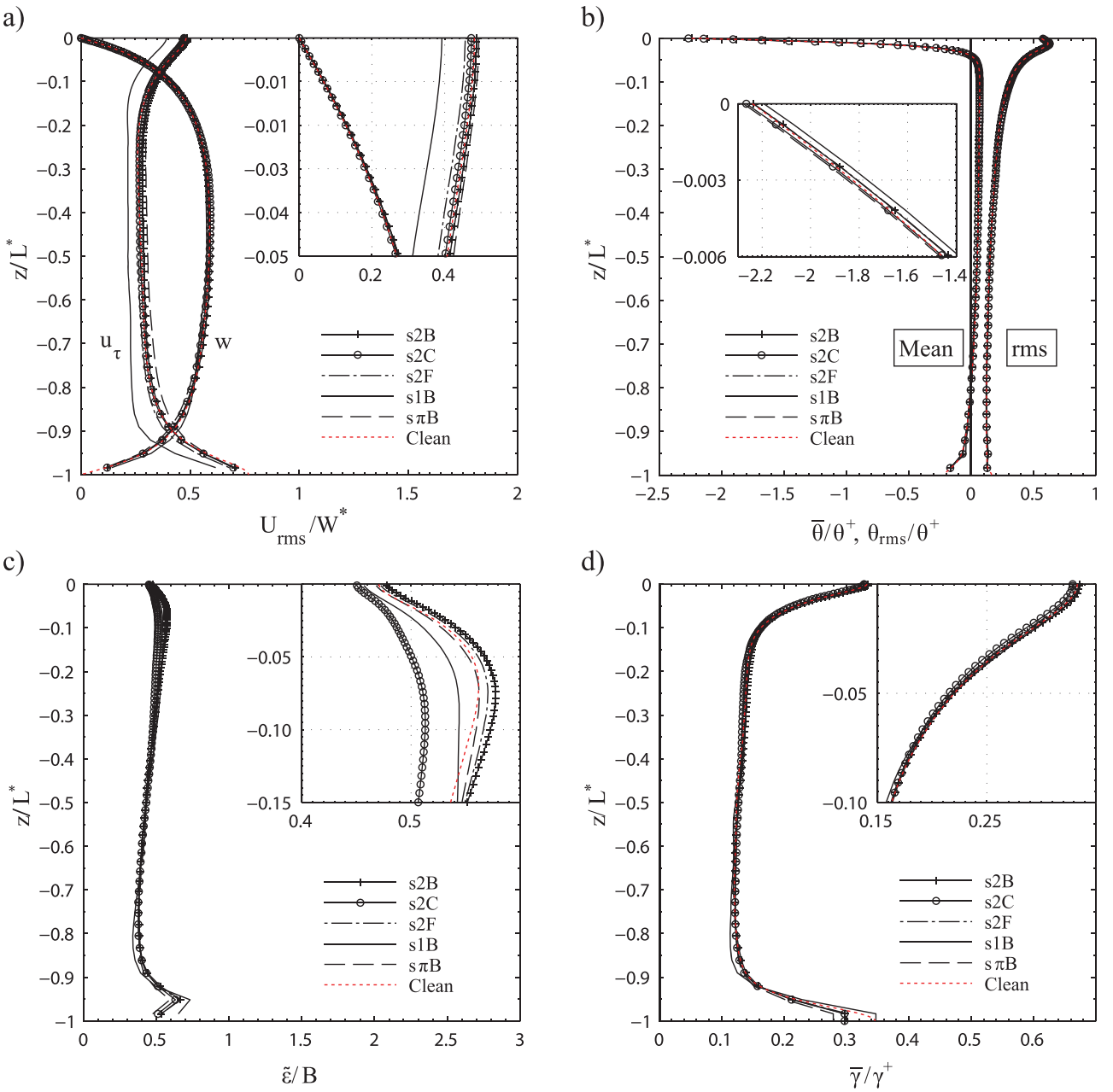

Figure 3. Present model and the *Clean* case from the pseudo-spectral model. (a) Vertical and horizontal rms velocity profiles where horizontal rms is defined as $(u_t)_{rms} = \left[(u_{rms}^2 + v_{rms}^2)/2\right]^{1/2}$ scaled with W^*. (b) Mean and rms temperature profiles scaled with θ^+. (c) Rate of turbulent kinetic energy dissipation scaled with the buoyancy flux, B. (d) Mean horizontal flow divergence is normalized with the inversed inner time scale, γ^+.

$$\bar{\sigma} = \frac{\sigma}{\sigma_0}, \quad \bar{\psi} = \frac{\psi}{\psi_0} \tag{34}$$

where σ, σ_0, ψ, and ψ_0 are the surface tension and surfactant concentration and their equilibrium values respectively. However, as discussed by *Handler et al.* [2003], another nondimensional number called the surfactant-turbulence interaction parameter is more descriptive of the underlying physics when a surfactant-covered surface interacts with the fluid motions below. It expresses the ratio of elastic to inertial forces as

$$\beta_E = \frac{E|_0}{\rho W^{*2} L^*} \tag{35}$$

where $E|_0 = -\psi_0 \left(\frac{d\sigma}{d\psi}\right)\Big|_0$ is the surface elasticity in equilibrium. This parameter is given for reference in Table 3 in which the cases in ZHF are summarized. The results from the sensitivity study of the surface velocity

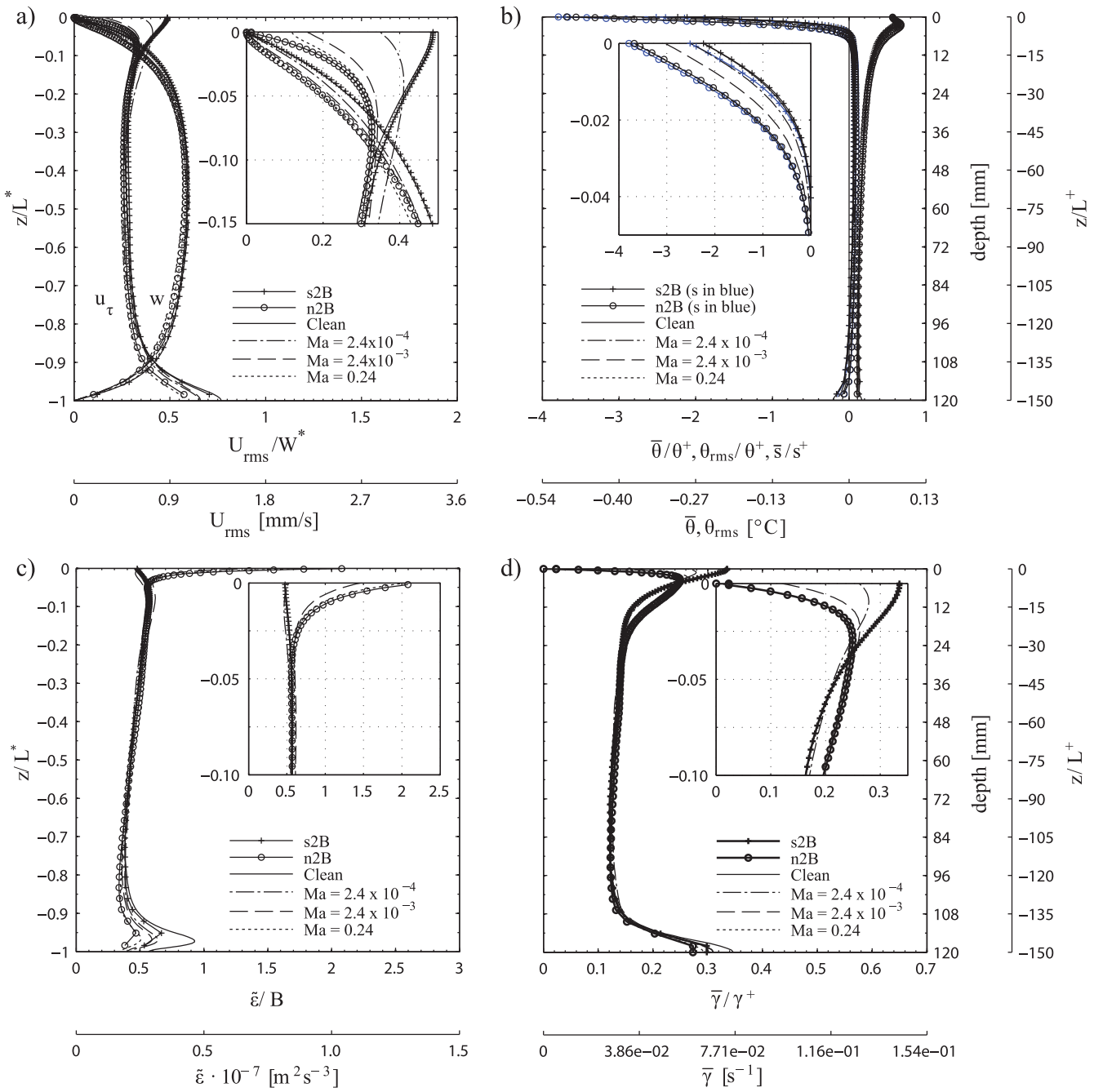

Figure 4. Present model with slip and no-slip boundary conditions and pseudo-spectral model with surfactant boundary condition respectively. The curves for Ma = 0.24 are difficult to see since they in general are on top of the no-slip curves. Nominal values are given for reference. (a) Vertical and horizontal rms velocity profiles where horizontal rms is defined as $(u_t)_{rms} = \left[\left(u_{rms}^2 + v_{rms}^2\right)/2\right]^{1/2}$ scaled with W^*. (b) Black: Mean and rms temperature profiles scaled with θ^+. Blue: Mean and rms scalar concentration (Sc=7) for slip and no-slip boundary condition scaled with s^+. (c) Rate of turbulent kinetic energy dissipation scaled with the buoyancy flux, B. (d) Mean horizontal flow divergence scaled with the inversed inner time scale, γ^+.

boundary condition are presented in Figure 4 in which there are both non dimensional and dimensional axes given for ease of interpretation.

The results show that a no-slip and a saturated surfactant surface boundary condition (high *Ma* number) give similar results for the rms vertical velocity, w_{rms}, the mean temperature, $\bar{\theta}$, the rms temperature, θ_{rms}, the turbulent kinetic energy dissipation, ε, and the rms horizontal flow divergence, γ_{rms}. The present study together with ZHF further suggest that there is a smooth transition from a clean surface, which is similar to

Table 3. Summary of Cases for Studies of a Surfactant Boundary Condition

Case	*Ma*	*E* (mNm)	β_E	*Q* (Wm^{-2})	L_x, L_y	L_z (m)	Resolution
Clean				100	$2L_z$	0.11731	128×128×129
Ma = 2.4×10^{-4}	2.4×10^{-4}	0.0132	0.0355	100	$2L_z$	0.11731	128×128×129
Ma = 2.4×10^{-3}	2.4×10^{-3}	0.132	0.355	100	$2L_z$	0.11731	128×128×129
Ma = 0.24	0.24	13.2	35.3	100	$2L_z$	0.11731	128×128×129

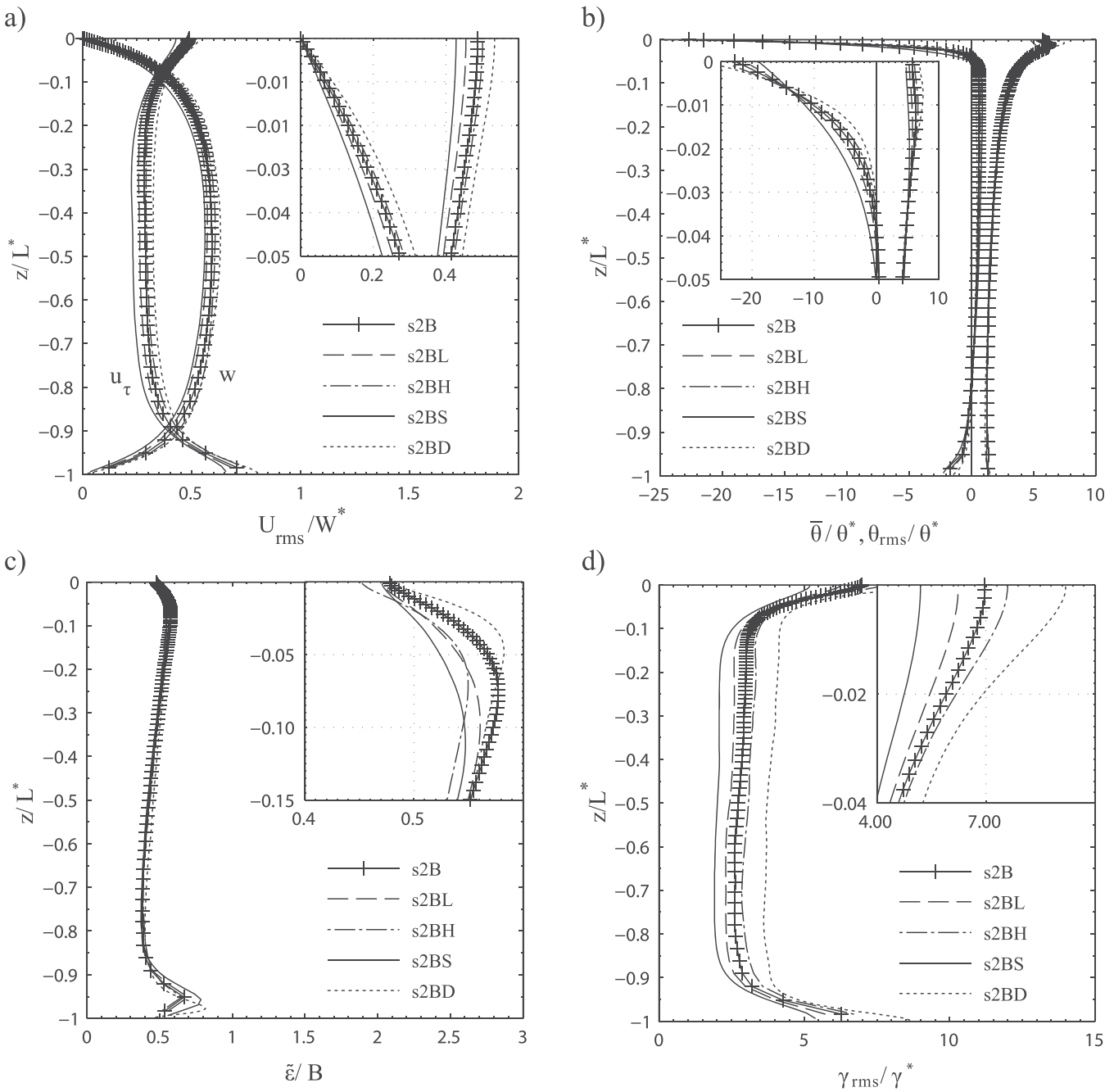

Figure 5. Present model with slip boundary conditions for the base case, *s2B*, the lower heat flux, *s2BL*, the higher heat flux, *s2BH, the* shallower domain, *s2BS*, and the deeper domain, *s2BD*, respectively. (a) Vertical and horizontal rms velocity profiles where horizontal rms is defined as $(u_t)_{rms}=\left[\left(u_{rms}^2+v_{rms}^2\right)/2\right]^{1/2}$ scaled with *w**. (b) Mean and rms temperature profiles scaled with θ^*. (c) Turbulent kinetic energy dissipation scaled with the buoyancy flux, *B*. (d) Rms horizontal flow divergence scaled with the inversed outer time scale, γ^*.

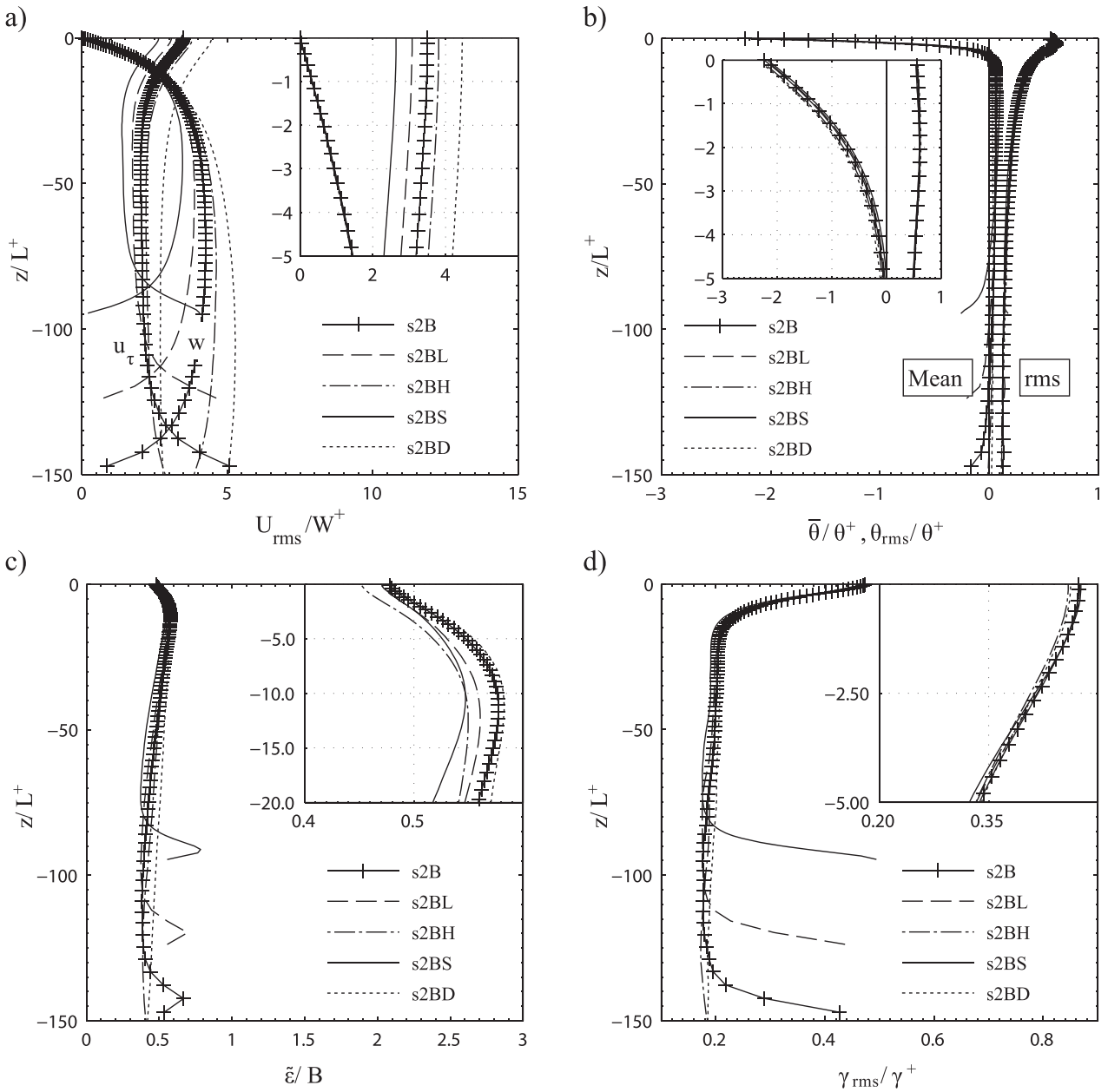

Figure 6. Present model with slip boundary conditions for the base case, *s2B*, the lower heat flux, *s2BL*, the higher heat flux, *s2BH*, the shallower domain, *s2BS*, and the deeper domain, *s2BD*, respectively. (a) Vertical and horizontal rms velocity profiles where horizontal rms is defined as $(u_t)_{rms}=\left[\left(u_{rms}^2+v_{rms}^2\right)/2\right]^{1/2}$ scaled with W^+. (b) Mean and rms temperature profiles scaled with θ^+. (c) Turbulent kinetic energy dissipation scaled with the buoyancy flux, *B*. (d) Rms horizontal flow divergence scaled with the inversed inner time scale, γ^+.

a slip boundary condition, to a saturated surfactant condition, which for most of the statistical averages is similar to a no-slip boundary condition. There is, however, still a difference in the rms of horizontal velocity $(u_\tau)_{rms}$ between the saturated surfactant boundary condition and the no-slip boundary condition since $(u_\tau)_{rms}$ is zero for the no-slip boundary condition while it is nonzero for the saturated case. The almost vanishing horizontal flow divergence for the saturated case in spite of the nonzero horizontal velocity can be understood by a decomposition of the horizontal flow into a solenoidal and an irrotational component [*Hasegawa and Kasagi*, 2008], where the latter is the dominating contributor to the flow divergence. Both components are zero for a no-slip boundary condition whereas a surfactant boundary condition mainly dampens the irrotational component while the solenoidal component is still nonzero.

Further, the no-slip case can favorably be compared to experimental results of nonpenetrative turbulent thermal convection [*Prasad and Gonuguntla*, 1996]. As is shown in Figure 4 the fluctuating vertical velocity

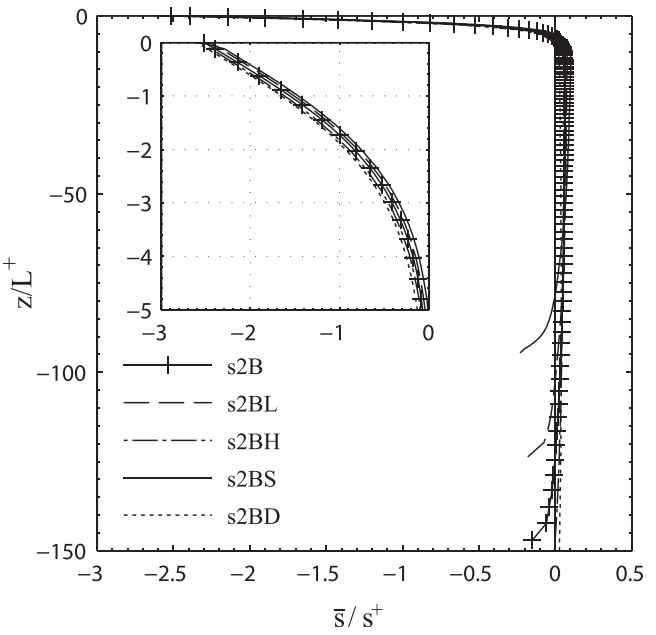

Figure 7. Mean scalar concentration normalized with s^+. Slip boundary surface conditions for the base case, *s2B*, the lower heat flux, *s2BL*, the higher heat flux, *s2BH*, the shallower domain, *s2BS*, and the deeper domain, *s2BD*, respectively.

in the present study, *s2B*, reaches its maximum value of $w_{rms}/W^* \approx 0.6$, which is close to the experimental value of $w_{rms}/W^* \approx 0.58$ at the same distance (i.e., $z/L_z \approx 0.35$) from the interface. The horizontal fluctuations at the same distance from the interface are $(u_\tau)_{rms}/W^* \approx 0.3$ in both the present study and in these measurements.

3.3. Different Surface Boundary Condition for Temperature and Scalar Concentration Field

This section will show to which extent the difference in surface boundary conditions for temperature and scalar fields affects the temperature and scalar-concentration gradients close to the surface. As explained in section 2.1 we use a constant gradient temperature boundary condition, which also can be interpreted as a constant heat flux across the surface, and a constant concentration boundary condition for the scalars. The assumption of a constant flux boundary condition for temperature is supported by comparing the results presented in Figure 2 and IR-measurement of surface temperature [i.e., *Kou et al.*, 2011; *Volino and Smith*, 1999]. The constant scalar concentration boundary condition is derived from the assumption that the horizontal concentration gradients at the air-water interface are much smaller in the air than in the water. Figure 4b shows the mean temperature (in black) and scalar concentration for $Sc=7$ (in blue) for slip and no-slip boundary conditions. It can be seen that the different boundary conditions for temperature and scalar concentration make a quantitative difference for the slip but not for the no-slip boundary conditions. The results are however qualitatively similar for both. This means that the heat flux can be used as a proxy for qualitative studies for flows driven by natural convection, keeping in mind the quantitative offset further discussed in section 3.5, for a scalar transport. This is very interesting out of two reasons: (i) The already very resource demanding calculations can, depending on the purpose of the calculation, be decreased by not solving for a passive scalar, and (ii) more importantly, the heat transfer velocity can be used to estimate the gas transfer velocity [*Jahne et al.*, 1987; *Lamont and Scott*, 1970; *Ledwell*, 1984; *Wanninkhof et al.*, 2009] according to equation (7).

3.4. Parameter Study of Varying Surface Heat Flux and Domain Depth

The statistics for the cases with varying surface heat flux and domain depths are presented in Figures 5–8 with different scaling in order to determine which scales are the most appropriate in different regions (e.g., inside and below the diffusive thermal and scalar sublayers). The vertical coordinates are made nondimensional with L^* in Figures 5 and 8a, and L^+ in Figures 6 and 8b, respectively. In Figure 8c the vertical coordinate is scaled with L^* in the full plot and L^+ in the inset. The rms velocity, mean and fluctuating temperature and horizontal flow divergence are scaled according to outer and inner scales in Figure 5 and 6 respectively, whereas the turbulent kinetic energy dissipation is scaled with the buoyancy flux in both figures. The mean scalar concentration is scaled with inner scaling in Figure 7. The turbulent heat and scalar transports are scaled with Q_0 and F_s in all the subplots in Figure 8 since $W^+\theta^+ = W^*\theta^* = Q_0$ and $W^+s^+ = W^*s^* = F_s$. The scalar transfer velocity for $Sc=7$ is shown in Figure 9. The zero-wind limit of the wind speed parameterizations k_{CC1998} in equation (2) and k_{W2009} in equation (3) for a gas with $Sc = 600$ are given for reference.

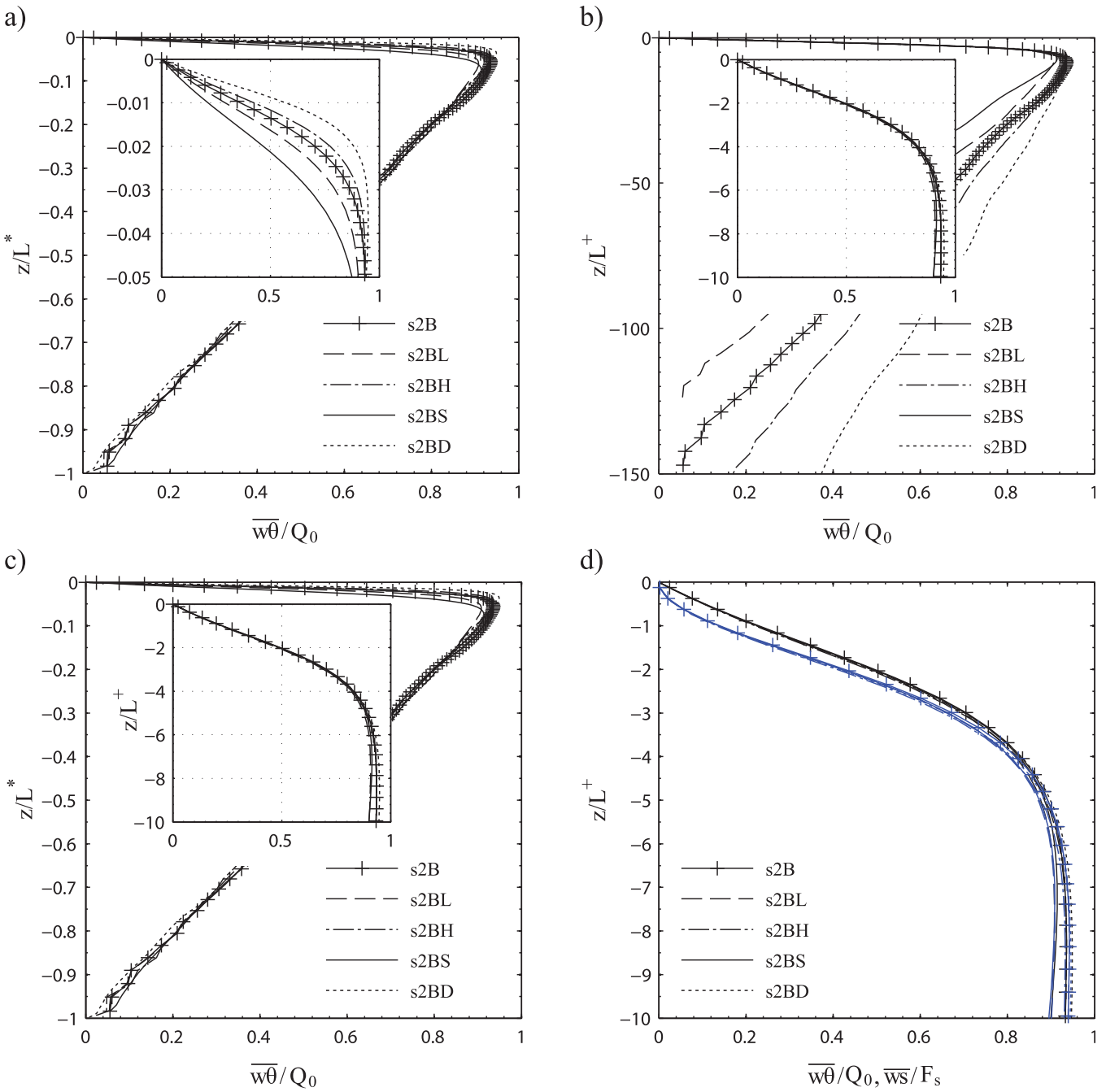

Figure 8. Vertical velocity-temperature correlation statistics. Present model with slip boundary conditions for the base case, *s2B*, the lower heat flux, *s2BL*, the higher heat flux, *s2BH*, the shallower domain, *s2BS*, and the deeper domain, *s2BD*, respectively. (a) Scaled with L^* and Q_0. (b) Scaled with L^+ and Q_0. (c) Length scaled generally with L^* and in the inset with L^+ and the velocity-temperature correlation with Q_0. (d) Vertical velocity-temperature and velocity-scalar-concentration correlation statistics, temperature in black and scalar concentration in blue. Scaled with L^+, Q_0 and F_s.

3.4.1. Surface Heat Flux

The heat flux parameter study consists of the base case *s2B* with dimensional heat fluxes of 100 Wm^{-2} ($Ra = 5 \cdot 10^8$), as well as one lower, *s2BL* (50 Wm^{-2}, $Ra = 2.5 \cdot 10^8$), and one higher, *s2BH* (200 Wm^{-2}, $Ra = 10 \cdot 10^8$), heat flux case.

In nature, the surface heat flux varies mainly due to different atmospheric forcing, e.g., evaporation rates, radiation, and clouds. Changing it can therefore be considered as a change in the environmental forcing at the surface. The depth profiles of the mean temperature and the fluctuating horizontal flow divergence

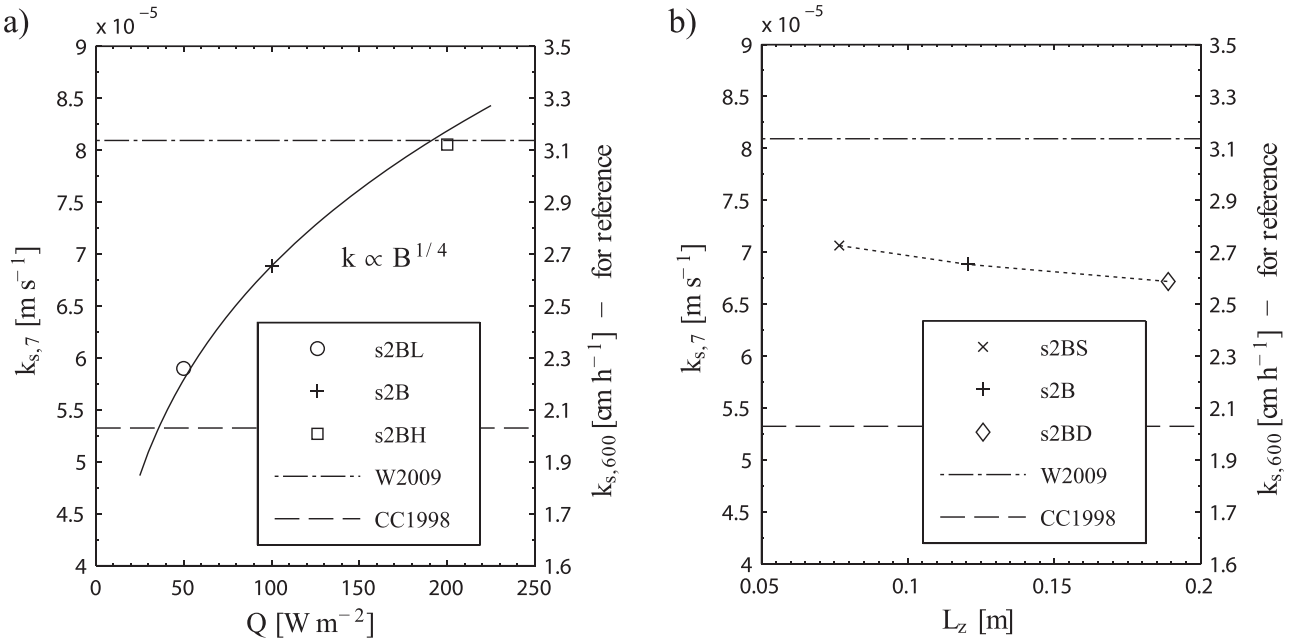

Figure 9. Scalar transfer velocities, k_s, for $Sc=7$ and compared to no-wind conditions for two parameterizations. Transfer velocities are converted between $k_{s,7}$ and $k_{s,600}$ with the exponent $n = 1/2$. (a) k_s as a function of the surface heat flux. (b) k_s as a function of the computational domain depth.

shown in Figures 6b and 6d scale well with the inner scales close to the surface. It is further shown in Figure 6c that the turbulent kinetic energy dissipation scales well with the buoyancy flux. Suitable scales for the velocity properties are more intriguing. The outer velocity scale is adequate for the horizontal velocity fluctuations all the way up to the surface, see Figure 5a, whereas it is more adequate to use inner and outer scaling for the vertical fluctuating velocity in and below the diffusive sublayer respectively (Figures 5a and 6a). The most appropriate length scales to use are L^+ within and L^* below the diffusive sublayer respectively. It is the fluctuations in the vertical velocity and the temperature and scalar concentrations that give the vertical turbulent heat and scalar transports. This is also apparent in Figure 8 where accordingly the

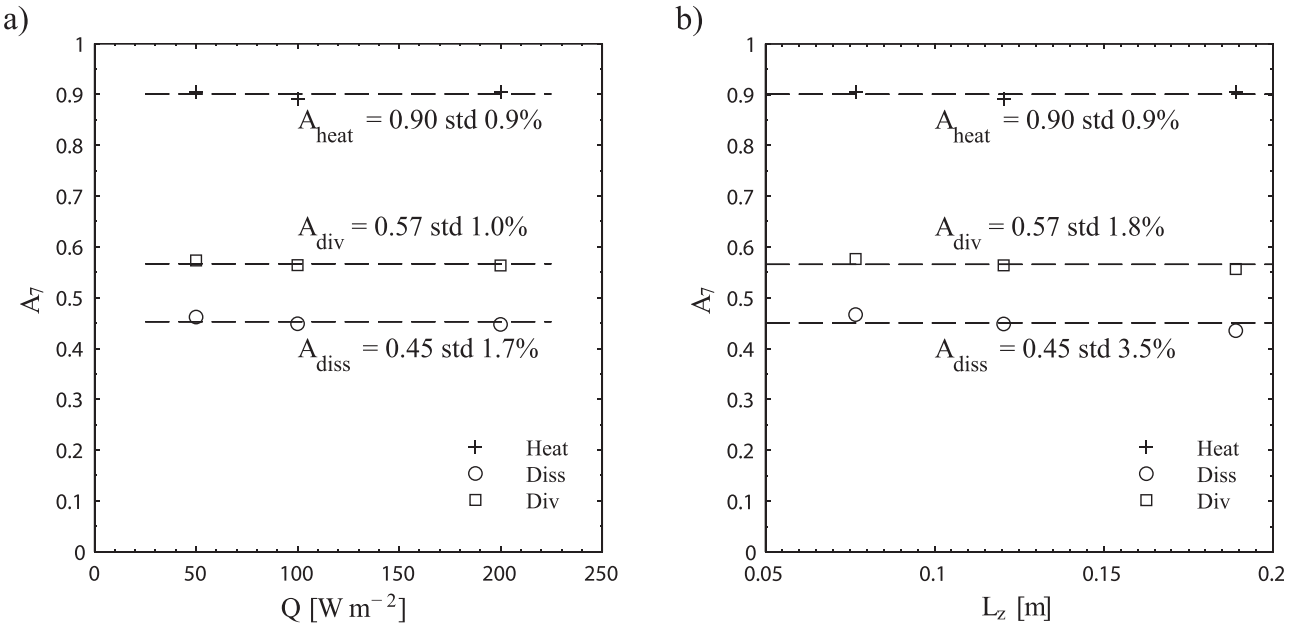

Figure 10. Transfer velocity constants, A, for $Sc=Pr=7$. The dashed lines are for each transfer constants. (a) A_7 as a function of the surface heat flux. (b) A_7 as a function of the computational domain depth.

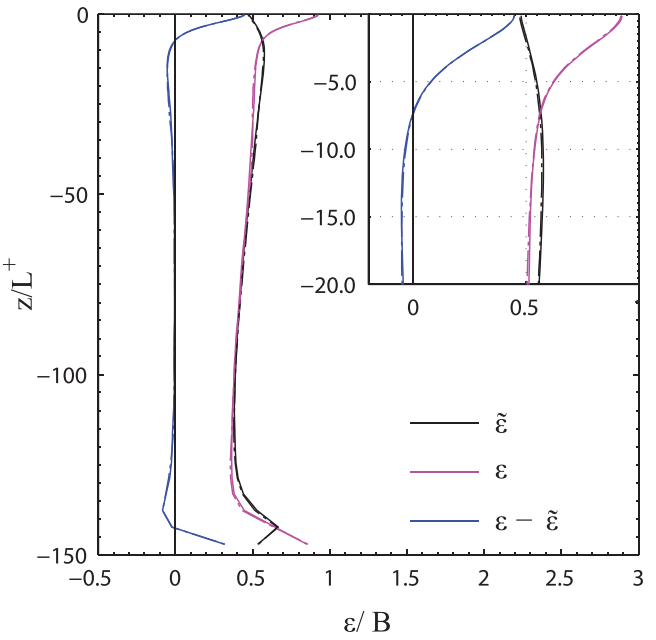

Figure 11. Rate of turbulent kinetic energy dissipation for case *s2B* (full line) and *s2F* (dash-dotted line). The results for *s2F* is difficult to see since the results for *s2B* and *s2F* are virtually the same. The pseudo-dissipation, $\tilde{\varepsilon}$, used for the calculation of A_{diss} is taken where $\tilde{\varepsilon}$ equals ε for the first time underneath the air-sea interface.

inner scales collapse the turbulent transport close to the surface. The dynamics in this region, which are important for the transport and therefore the transfer velocity, should therefore be scaled with the inner scales. The inner scales include a buoyancy flux dependence, $B^{1/4}$, and it is therefore not surprising that the transfer velocity shown in Figure 9a scales very well with $Q^{1/4}$. This heat flux dependency also matches the theory associated with the dissipation method [*Lamont*, 1960; *Zappa et al.*, 2007] given that the rate of turbulent kinetic energy dissipation via the buoyancy flux is a function of the heat flux.

3.4.2. Domain Depth

Three different domain depths L_z are used, including that of the base case *s2B* ($L_z = L_{zB}$, $Ra = 5 \cdot 10^8$), a shallower domain in case *s2BS* ($L_z = 2L_{zB}/\pi$, $Ra = 0.8 \cdot 10^8$) and a deeper domain in case *s2BD* ($L_z = \pi L_{zB}/2$, $Ra = 30 \cdot 10^8$). Figures 5a and 6a show the fluctuating vertical and horizontal velocities for these cases. It can be seen that $(u_\tau)_{rms}$ scales well with W^* both below and within the diffusive boundary layer, whereas w_{rms} only scales with W^* below the diffusive boundary layer. Within the diffusive boundary layer the data collapse well when using W^+ and L^+ as velocity and depth scales, respectively, which once again shows the relevance of the inner scaling near the boundary. There is however even for outer scaling a small increase in $(u_\tau)_{rms}/W^*$ with increasing domain depth. It is further seen in Figures 5b, 5c, 6b, and 6c that the temperature profile and the turbulent kinetic energy dissipation scales well with θ^+ and the buoyancy production B, respectively. The rms horizontal flow divergence is shown, in Figures 5d and 6d, to scale well with inner scales inside the diffusive boundary layer. It is in general seen in Figures 5 and 6 that inner scaling works better than outer scaling close to the surface.

The domain depth in our simulations does to some degree correspond to the mixed layer depth of a natural system, and altering the domain depth can therefore be considered as altering the mixed layer depth. The small depths used here compared to those in natural systems raises the natural question as to whether the results of the present study can be expected to say anything about natural mixed layers. The fact that our results follow the inner scaling so well for the chosen range of domain depths, lends support to our hypothesis that this is the case even for larger domain depths (larger Rayleigh numbers). This has important implications for the transfer velocities, since these are then independent of the domain depth, for sufficiently large depths. The scalar transfer velocities are shown in Figure 9b to be relatively constant for the chosen range of domain depths. There is a small, counterintuitive, increase for the shallowest domain case, which may be an indication that the depth has some influence for that case, but the two larger depth cases seem to be sufficiently deep.

A number or papers [e.g., *Macintyre et al.*, 2002; *Read et al.*, 2012; *Rutgersson et al.*, 2011] discuss a buoyancy velocity, $W^* = (BL_z)^{1/3}$, dependence in the mass transfer velocity. An increase of $W^* \propto L_z^{1/3}$ would then imply an increase of the gas transfer velocity for an increasing layer depth, L_z. It can, however, be concluded that the present study does not support an increase of the transfer velocity as a function of depth, which would be implied by a W^* scaling.

3.5. Estimates of Mass Transfer Velocity

The scalar transfer velocity, k_s, (see equation (15)) is used as a measure to study the parameterization methods discussed above in section 1.1 by establishing the constants in equations (5–7) given by:

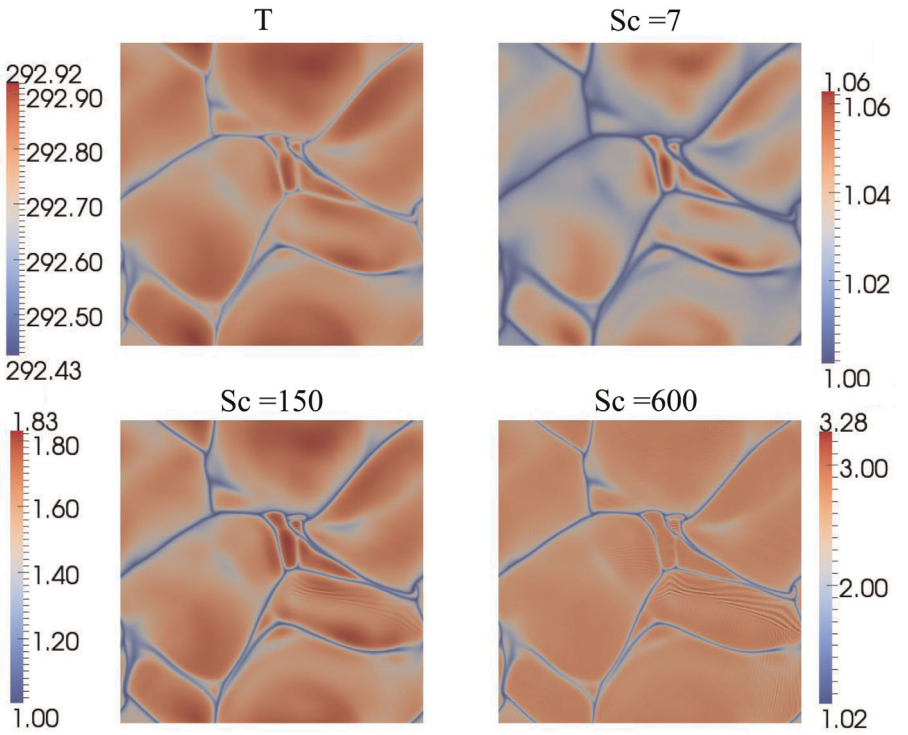

Figure 12. Temperature and scalar concentration fields, for $Sc = 7$, $Sc = 150$ and $Sc = 600$, for slip boundary conditions for the fine, *s2F*, mesh resolution.

$$A_{diss,Sc} = \frac{k_{s,Sc}}{(\varepsilon\nu)^{1/4}} Sc^n, \tag{36}$$

$$A_{div,Sc} = \frac{k_{s,Sc}}{\sqrt{\gamma_{rms}\,\nu}} Sc^n, \tag{37}$$

and

$$A_{heat,Sc} = \frac{k_{s,Sc}}{\kappa_{heat}} \left[\frac{Pr}{Sc}\right]^{-n}. \tag{38}$$

The constants, for a scalar with $Sc = 7$, are calculated by the method of least squares for the cases with varying heat flux (*s2BL*, *s2B*, and *s2BH)* and varying domain depth (*s2BS, s2B*, and *s2BD)* respectively. They are given together with their standard deviations in Figures 10a and 10b.

3.5.1. Wind Parameterizations

The present work shows that there is a scalar transport also for no-wind conditions driven by natural convection. This contradicts some of the wind parameterizations [*Bade*, 2009] which show a zero transfer velocity for no-wind conditions. Figure 9a shows that the two wind parameterizations of the gas transfer velocity chosen in the present study result in fairly good predictions using $n = 1/2$ for a surface heat flux of 100 Wm^{-2}. One [*Cole and Caraco*, 1998] underpredicts the transfer velocity, corresponding to a heat flux of 35 Wm^{-2} and the other [*Wanninkhof et al*., 2009] overpredicts the velocity corresponding to a heat flux of 200 Wm^{-2}.

3.5.2. Turbulent Kinetic Energy Dissipation

In the present study the rate of turbulent kinetic energy dissipation to be used in equation (5) is taken at the depth of the viscous sublayer defined as the smallest depth where the pseudo-dissipation, $\tilde{\varepsilon}$, and the true viscous dissipation, ε, are identical, see Figure 11. It can be seen in Figure 11 that $\tilde{\varepsilon}$ as well as ε are virtually the same for the base mesh *s2B* (full line) and the fine mesh case *s2F* (dash-dotted line). It can further be noticed from earlier sections, Figure 3c, that $\tilde{\varepsilon}$ is within $\pm 1\%$ for *s2b*, *s2F*, and *Clean*. This implies that these calculations, as the pseudo-spectral code used in *Clean*, are enough resolved to capture $\tilde{\varepsilon}$ and give robust values of A_{diss}. If needed, the dissipation can be measured at a greater depth and then be

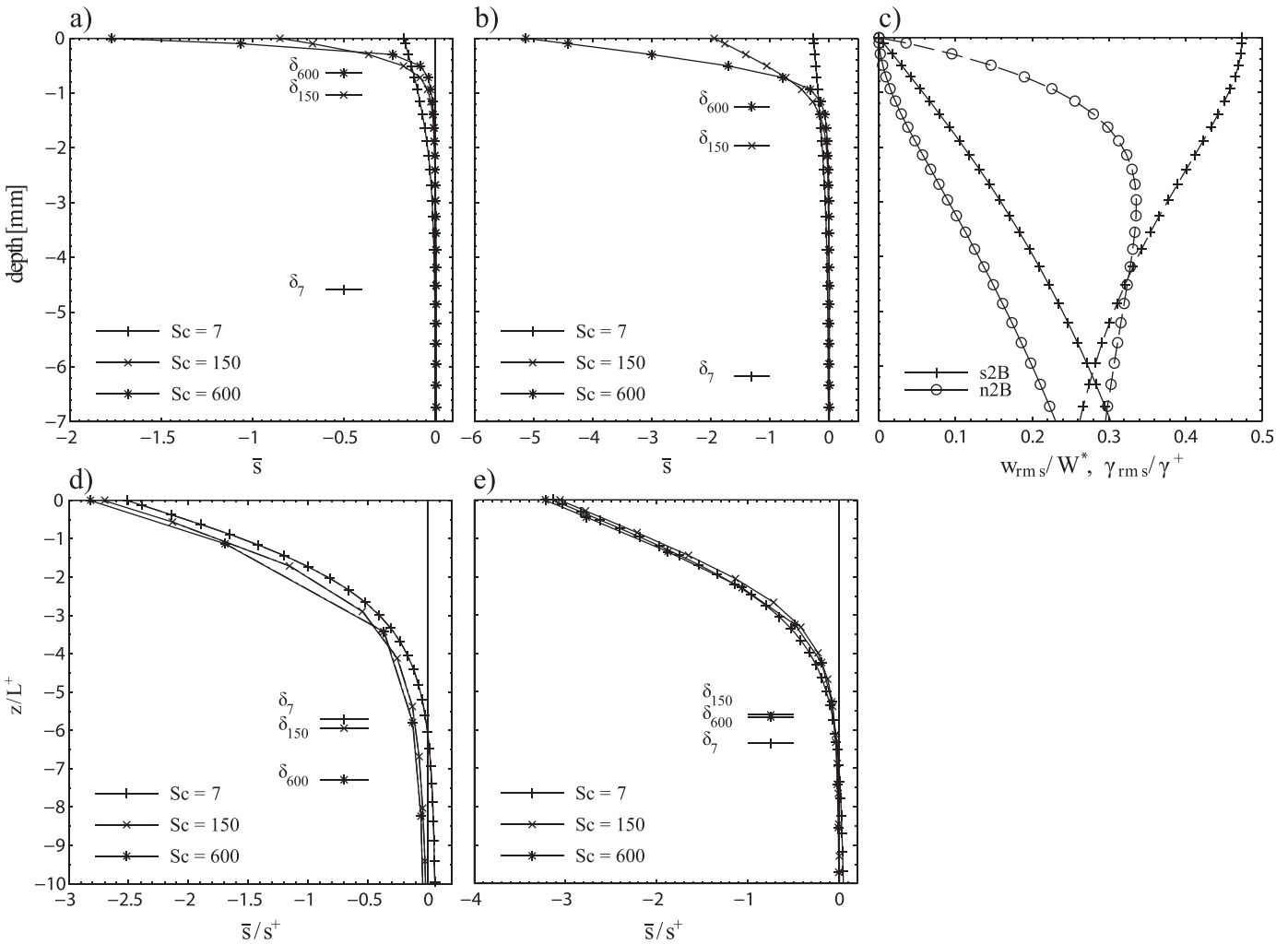

Figure 13. Mean scalar concentration, fluctuating vertical velocity and fluctuating horizontal flow divergence for slip and no-slip boundary conditions. Concentrations and the sublayer depths, δ, are given for scalars with *Sc* numbers equal to 7, 150, and 600. (a) Slip boundary conditions, the results for *s2B* (full line) and *s2F* (dash-dotted line) are very similar and therefore difficult to distinguish in the plot. (b) No-slip boundary conditions, *n2B*. (c) Slip and no-slip boundary conditions: left (solid line) - rms of vertical velocity; right (dashed line) - rms horizontal flow divergence. (d, e) As Figures 13a and 13b but scaled with inner scales L^+ and s^+.

extrapolated to the appropriate sublayer depth. It can however be seen in Figure 5c that since the transfer velocity is a function of the turbulent kinetic energy dissipation as $\varepsilon^{1/4}$ the actual depth where the pseudo-dissipation is monitored only alters the results by a few percent for the present flow cases. The present study gives A_{diss}=0.45, see Figure 10, for the slip case ($A_{diss} \approx 0.4$ for true viscous dissipation at the surface). This can be compared to A_{diss}=0.4 [*Lamont and Scott*, 1970], and A_{diss}=0.42 previously quantified through field experiments [*Zappa et al*., 2007]. For the no-slip case (not shown) the constant is A_{diss}=0.41 for $Sc = 7$ and $Pr = 7$.

3.5.3. Divergence

A number of derivations have presented a relationship between the mass transfer velocity and the horizontal flow divergence, see equation (6). Most of them as well as the present study use the rms values of the horizontal flow divergence. The results in present work give A_{div}=0.57, see Figure 10, where the rms of the horizontal divergence is measured at the surface. This can for a clean surface be compared to analytical work by *Ledwell* [1984] and *Mccready et al*. [1986] resulting in A_{div}=0.64 and A_{div}=0.71 respectively. Experimental work has resulted in A_{div}=0.5 [*McKenna and McGillis*, 2004] and A_{div}=0.45 [*Turney et al*., 2005] for both clean and contaminated surfaces. For no-slip boundary conditions the vertical gradient of the horizontal flow divergence can be used to estimate k_g [*Ledwell*, 1984]. This gradient is however difficult to measure in the field and has therefore not been evaluated in the present work.

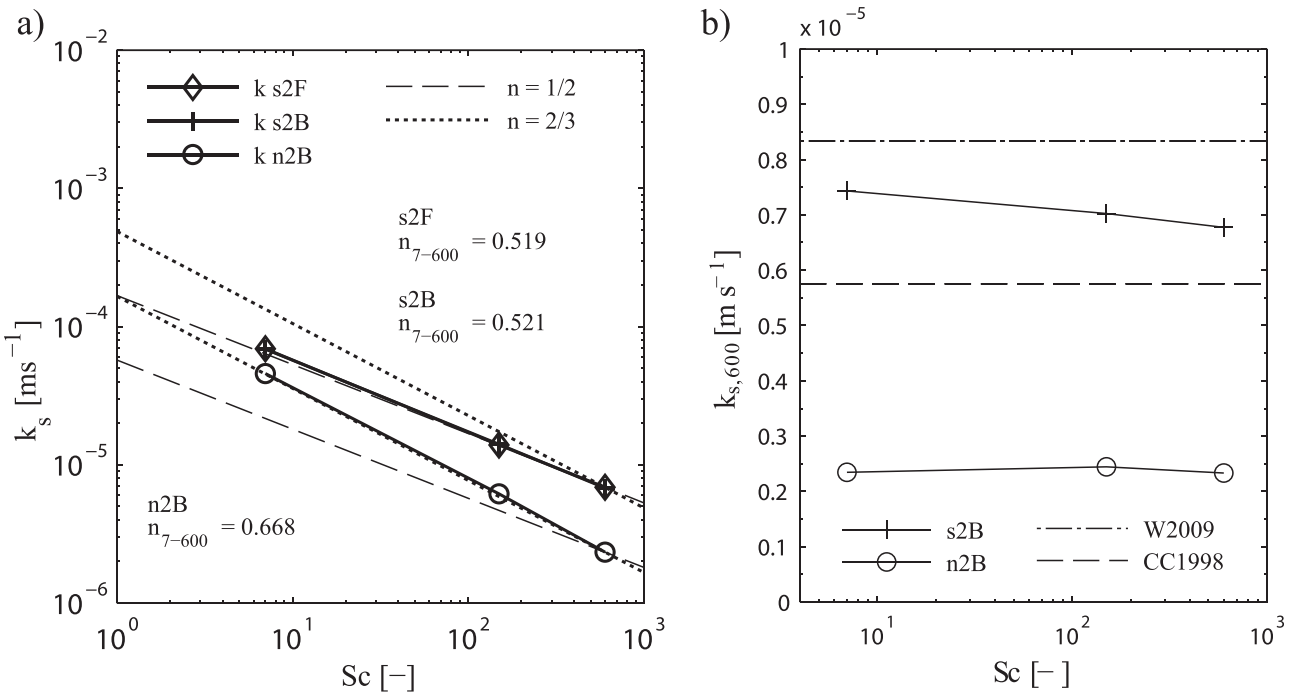

Figure 14. (a) Scalar transfer velocity for case *s2B, s2F*, and *n2B* with three passive scalars with Schmidt number $Sc = 7$, $Sc = 150$ and $Sc = 600$ respectively. The results for the base (*s2B*) and the fine (*s2F*) mesh resolution are difficult to distinguish since they are very similar. Dashed and dotted lines corresponds to $n = 1/2$ and $n=2/3$ and originate from $k_{s,600}$ for the slip and no-slip boundary condition case respectively. (b) The transfer velocities for the slip and no-slip boundary conditions are scaled with n of 1/2 and 2/3, respectively. The wind parameterizations are scaled with $n = 1/2$.

3.5.4. Heat Flux

The heat transfer velocity can be used [*Frew et al*., 2004] to find the gas transfer velocity according to equation (7) where ΔT in the present study is defined as the difference between the temperature at the surface and its maximum value (at the depth where the vertical gradient is zero). It is shown in Figure 10 that $A_{heat} = 0.90$ for all cases with $Sc = 7$ and $Pr = 7$. This means that by estimating the gas exchange from the heat flux without using the A_{heat} one will overestimate the gas flux with 11% before any uncertainty due to the *Sc* number conversion is taken into account.

3.6. Passive Scalars with Different Schmidt Numbers

The temperature and scalar concentration fields for $Sc = 7,\ 150$, and 600 for the case *s2F* with slip boundary conditions at the surface, are presented in Figure 12. It is shown that the horizontal scalar-concentration gradients within the thinner plumes are increasing with increasing Schmidt number. The fields are plotted just below the surface ($z=-0.4$ mm$=3.3 \cdot 10^{-3}\ L^*$) since the scalar concentration is constant at the surface. Some numerical oscillations are present for the scalars with high Schmidt numbers in the same way as for the temperature in the coarse mesh case, *s2C*, see Figure 2. It is however shown in section 3.1 that the mean temperature gradient close to the surface, and the diffusive sublayer depth were well captured even though there were oscillations present in the temperature field in *s2C*. This gives reason to believe that the diffusive sublayer depth and the scalar transfer velocity can be studied also for higher Schmidt numbers (although resulting in numerical oscillations at the surface) in the present work. This is further supported in Figure 13 where results from *s2B*, *s2F* and *n2B* are presented. Here, it is shown in Figures 13a and 13d that *s2B* (full line) and *s2F* (dash-dotted line) give virtually the same results for the mean scalar concentration. The vertical resolution for high *Sc* numbers was evaluated (not shown) using a mesh that was refined by two in all directions compared to the mesh resolution in *s2B*. The computational domain aspect-ratio was reduced to 1:1 due to computational resource limitations. The scalar transfer velocity showed a variation less than 1% for $k_{s,7}$, $k_{s,150}$, and $k_{s,600}$ respectively. A higher resolution would resolve the smallest scales for $Sc = 600$ better but would most likely not influence the scalar transfer velocity significantly.

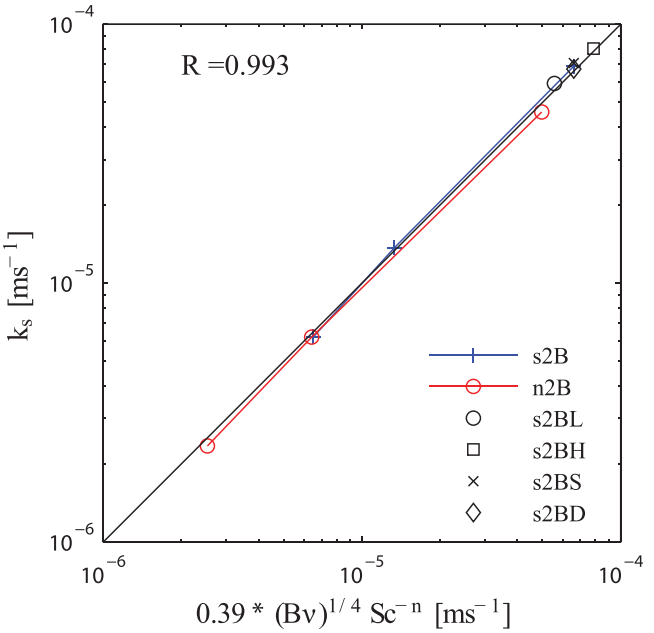

Figure 15. Scalar transfer velocity versus modeled k_s as determined from equation (39). Case *s2B* and *n2B* include the *Sc* numbers 7, 150, and 600.

Figures 13a–13c show the mean scalar concentrations, w_{rms}/W^*, and γ_{rms}/γ^+ as a function of depth. Figures 13d and 13e show the mean scalar concentrations normalized with inner scaling. For *s2B* and *n2B*, the scalar diffusive sublayer depths, $\delta_{s,7}$, $\delta_{s,150}$, and $\delta_{s,600}$, here defined following *Leighton et al.* [2003] as the depth where the molecular diffusion accounts for 5% of the total flux for, are used to demonstrate how the Schmidt number affects the sublayer thickness.

It is seen in Figures 13a and 13b that the vertical gradients for the mean scalar concentration with $Sc = 150$ and even more so for $Sc = 600$ are much larger than for the scalar with $Sc = 7$. The theoretical predictions of the *Sc* number dependency in e.g., *Ledwell* [1984] assume that w_{rms} increase linearly and quadratic with distance from the surface for slip, and for no-slip conditions respectively. Figure 13c shows in accordance with these assumptions that w_{rms} show a quadratic and a linear dependence for small depths. It is however also seen that these dependencies are becoming linear for both no-slip and slip boundary conditions as the depth approaches the diffusive boundary layer thickness for a scalar with $Sc=7$. The *Sc* number dependency for slip and no-slip conditions obtained here support the theoretical derivations ($n=1/2$ and $2/3$ respectively) for *Sc* numbers ranging from 7 to 600. It can therefore be concluded that it is the processes at the very vicinity of the surface that controls the transfer velocity since w_{rms} for no-slip actually shows a linear relationship with depth for a large part of the diffusive boundary layer depth. These results should be taken with some caution since the diffusive boundary layer is rather coarsely resolved at the highest *Sc* number ($Sc=$ 600, Figure 13), especially for the slip case (Figures 13a and 13d). On the other hand, the main deviations from these power laws would be expected to exist for no-slip boundary conditions at low *Sc* numbers (no oscillations present) where the diffusive boundary layer is thick and the theoretical assumptions are the least appropriate.

The scalar concentrations and vertical coordinates have in Figures 13d and 13e been scaled with inner scales which collapse the results for both the slip and the no-slip boundary cases. This shows the relevance of the proposed scaling, but also is an indirect proof of the eddy cell model given in equation (5) and to some extent the surface divergence model given in equation (7) in the case of natural convection. Again, the results at $Sc=600$ should be taken with some caution due to the low vertical resolution of the diffusive boundary layer for this scalar (Figures 13a and 13d).

The scalar transfer velocities for the cases with slip and no-slip boundary conditions, *s2B, s2F*, and *n2B*, are given as a function of the scalar Schmidt number in Figures 14a and 14b. It is shown that the Schmidt number dependence gives an exponent *n* close to 1/2 (0.521 and 0.519 for *s2B* and *s2F* respectively) and 2/3 (0.67) for the slip and the no-slip boundary conditions respectively. In Figure 14a, the *Sc* number dependencies for *n* equal to $1/2$ and $2/3$ with $Sc=600$ as a nominal value are given for reference for both the slip and the no-slip boundary conditions respectively. Earlier studies [e.g., *Papavassiliou and Hanratty*, 1997] have shown a change in the Schmidt number exponent for $Sc = \mathcal{O}(10^1)$, which is not supported by our results. In Figure 14b the transfer velocities are scaled with exponent *n* equal to $1/2$ and $2/3$ for the slip and the no-slip boundary conditions respectively. The wind speed estimates, converted to different Schmidt numbers with $n=1/2$, are given for reference. The scalar transfer velocity ratio between the slip and no-slip boundary-condition case is approximately 0.65 and 0.34, for the scalars with $Sc=7$ and 600 respectively, which for the high Schmidt number matches values found by *McKenna and McGillis* [2004] for gas transfer velocities

for clean and contaminated surfaces. Note that the results for fine and base horizontal resolution are close to similar ($k_{s,7}$, $k_{s,150}$, and $k_{s,600}$ differ 0.3%, 1.2% and 1.3% between *s2B* and *s2F*) which once again indicates that the mesh resolution is sufficient for estimating the scalar transfer velocity also for the scalars with higher *Sc* numbers.

3.7. A New Expression for Mass Transfer Velocities Under Natural Convective Forcing

It is shown in Figures 7, 8d, 13d, and 13e that the inner velocity scaling $W^+ = Sc^{-n}(Bv)^{1/4}$, the length scaling $L^+ = Sc^{n-1}\left(\frac{v^3}{B}\right)^{1/4}$ and scalar concentration scaling $s^+ = F_s Sc^n (Bv)^{-1/4}$ can be used to collapse the scalar concentration profiles for varying surface heat flux, domain depths, and *Sc* numbers. It can be seen that all these inner scales include *Sc*, *n*, v, and *B* but not the domain depth. It is therefore natural to arrange the variables in these scaling to find an expression using equation (10) for the scalar transfer velocity as

$$k_s = 0.39\ (Bv)^{1/4}\ Sc^{-n} \tag{39}$$

Here the constant 0.39 is the mean value for all the cases in the heat flux, domain depth, and *Sc* number sensitivity analyses which is plotted in Figure 15.

4. Summary and Conclusions

A finite volume DNS model is used to study the heat and gas exchange caused by natural convection in the water. The gas exchange is modeled using a passive scalar transport. The finite-volume method used here and a pseudo-spectral method (ZHF) give very similar results for comparable runs, which implies that the different codes give robust results. The numerical results also compare favorably with experimental studies. It is found that a domain ratio with the horizontal length twice the depth is enough to capture the heat and scalar flux phenomena of interest.

The velocity surface boundary conditions in the present study are either slip or no-slip whereas ZHF used a surfactant model with a blend of different Marangoni numbers ranging from a clean surface to a surface saturated with surfactants. The combined results show a smooth transition from the slip to the no-slip boundary condition case for mean and rms of temperature and velocity (with a small deviation for rms horizontal velocity), rate of turbulent kinetic energy dissipation, and horizontal divergence. This implies that the no-slip boundary condition can be used to model gas exchange from a surfactant saturated surface.

The scalar transfer velocity is shown to decrease with increasing Schmidt number as $k_s \propto Sc^{-n}$ with $n=0.52$ for slip and $n=0.67$ for no-slip surface boundary conditions. This follows theoretical derivations of the Schmidt number dependency, [i.e., *Ledwell*, 1984], suggesting $n=1/2$ and $n=2/3$. A cornerstone in the derivation by *Ledwell* [1984] is the assumption of linear and quadratic relationships between the rms vertical velocity and the depth close to the surface for slip and no-slip boundary conditions, respectively. The present study shows that these relationships are only valid for the uppermost fraction of the diffusive boundary layer and are then linear in the main part of the diffusive boundary layer for both slip and no-slip boundary conditions. This is especially true at low Schmidt numbers with thicker diffusive boundary layers. This indicates that it is the processes in this uppermost fraction of the diffusive boundary layer that controls the transfer velocity.

Although the surface boundary conditions for temperature (constant heat flux) and the scalar concentration (constant concentration) are different, the temperature and scalar gradients for $Pr=Sc=7$ give qualitatively similar results which imply that the heat transfer velocity can be used as a proxy for the scalar transport velocity. It should though be kept in mind that *Sc* is two magnitudes higher for typical greenhouse gases as C_2O and CH_4 in water. The actual gas transfer velocity for these gases must therefore be estimated through the *Sc* dependence. This conversion gives an uncertainty in the scalar transfer velocity estimate since the dependence (*n*-exponent) is sensitive to surfactants as can be seen in the paragraph above.

The scalar transfer velocity $k_s \propto Q^{1/4}$ which is in agreement with inner scaling and supports the buoyancy flux dependency in equation (39). There is no domain depth dependence in the scalar transfer velocity for increasing domain depth. There is, however, a small increase of the scalar transfer velocity for the smallest depth but this is most likely due to a low *Ra* number effect that is not present for the two larger depths. It is shown that inner scaling collapses many of the important dynamics (i.e., rms vertical velocity, mean temperature and scalar concentration, surface flow divergence, and turbulent transport) for the transfer velocity

close to the surface. A no-depth dependency implies that the present results are relevant for natural systems, also from a domain depth point of view. It also contradicts an inclusion of a convection velocity, $W^* = (BL_z)^{1/3}$ which has a depth dependency, as is done in some parameterizations of the gas transfer velocity. Our results show that the scalar transfer velocity for convective forcing can be parametrized as $k_s = 0.39 (Bv)^{1/4} Sc^{-n}$ for varying surface heat flux, domain depth, surface velocity-boundary conditions, and *Sc* number. One may note that the present parameterization gives values comparable with some wind parameterizations at $U_{10} \approx 3\ ms^{-1}$ at reasonable heat losses from the surface, so it is reasonable to assume that convection is important below at least such wind speeds.

The present work thus shows that there is a nonzero scalar flux due to convection for no-wind conditions. This flux is not included in some earlier parameterizations. It is further shown that the two wind parameterizations of the gas transfer velocity chosen in the present study result in fairly good estimates using $n = 1/2$ for a surface heat flux of 100 Wm^{-2}. One [*Cole and Caraco*, 1998] corresponds to a heat flux of 35 Wm^{-2} and the other [*Wanninkhof et al.*, 2009] corresponds to a heat flux of 200 Wm^{-2}. The other three parameterizations (dissipation, divergence and heat flux) succeed in estimating scalar transport within an error of 4% for all cases, with parameterization constants that correspond well with those given in the literature.

Acknowledgments

The computations were performed on resources provided by the Swedish National Infrastructure for Computing (SNIC) at C3SE (Chalmers Centre for Computational Science and Engineering) computing resources. The open source code for the general computational fluid dynamics model used in this study, the OpenFOAM 2.1.x, is freely available at http://www.openfoam.org/archive/2.1.0/download/git.php. The adaption source code and the input files necessary to reproduce the present DNS with OpenFOAM, are available from the authors upon request (sam.fredriksson@gu.se).

References

Adrian, R. J., R. T. D. S. Ferreira, and T. Boberg (1986), Turbulent thermal-convection in wide horizontal fluid layers, *Exp. Fluids*, *4*(3), 121–141.

Asher, W. E., H. Z. Liang, C. J. Zappa, M. R. Loewen, M. A. Mukto, T. M. Litchendorf, and A. T. Jessup (2012), Statistics of surface divergence and their relation to air-water gas transfer velocity, *J. Geophys. Res.*, *117*, C05035, doi:10.1029/2011JC007390.

Bade, D. L. (2009), Gas exchange at the air–water interface, in *Encyclopedia of Inland Waters*, edited by G. E. Likens, pp. 70–78, Academic, Oxford, U. K., doi:10.1016/B978-012370626-3.00213-1.

Banerjee, S., D. S. Scott, and E. Rhodes (1968), Mass transfer to falling wavy liquid films in turbulent flow, *Ind. Eng. Chem. Fundam.*, *7*(1), 22, doi:10.1021/I160025a004.

Banerjee, S., D. Lakehal, and M. Fulgosi (2004), Surface divergence models for scalar exchange between turbulent streams, *Int. J. Multiphase Flow*, *30*(7-8), 963–977, doi:10.1016/j.imultiphase.2004.05.004.

Bastviken, D., L. J. Tranvik, J. A. Downing, P. M. Crill, and A. Enrich-Prast (2011), Freshwater methane emissions offset the continental carbon sink, *Science*, *331*(6013), 50–50, doi:10.1126/science.1196808.

Calmet, I., and J. Magnaudet (1998), High-Schmidt number mass transfer through turbulent gas-liquid interfaces, *Int. J. Heat Fluid Flow*, *19*(5), 522–532, doi:10.1016/S0142-727x(98)10017-6.

Ciais, P., et al. (2013), Carbon and other biogeochemical cycles, in *Climate Change 2013: The Physical Science Basis. Contribution of Working Group I to the Fifth Assessment Report of the Intergovernmental Panel on Climate Change*, edited by T. F. Stocker, et al., pp. 465–570, Cambridge Univ. Press, Cambridge, U. K., doi:10.1017/CBO9781107415324.015.

Cole, J. J., and N. F. Caraco (1998), Atmospheric exchange of carbon dioxide in a low-wind oligotrophic lake measured by the addition of SF6, *Limnol. Oceanogr.*, *43*(4), 647–656

Cole, J. J., et al. (2007), Plumbing the global carbon cycle: Integrating inland waters into the terrestrial carbon budget, *Ecosystems*, *10*(1), 171–184, doi:10.1007/s10021-006-9013-8.

Csanady, G. T. (1990), The role of breaking wavelets in air-sea gas transfer, *J. Geophys. Res.*, *95*(C1), 749–759, doi:10.1029/JC095ic01p00749.

Deardorf, J. W. (1970), Convective velocity and temperature scales for unstable planetary boundary layer and for Rayleigh convection, *J. Atmos. Sci.*, *27*(8), 1211, doi:10.1175/1520-0469(1970)027<1211:CVATSF>2.0.CO;2.

Donelan, M. A., and R. Wanninkhof (2002), Gas transfer at water surfaces—Concepts and issues, in *Gas Transfer at Water Surfaces*, edited by M. A. Donelan et al., pp. 1–10, AGU, Washington, D. C., doi:10.1029/GM127p0001.

Fortescue, G. E., and J. R. A. Pearson (1967), On gas absorption into a turbulent liquid, *Chem. Eng. Sci.*, *22*(9), 1163, doi:10.1016/0009-2509(67)80183-0.

Frew, N. M., et al. (2004), Air-sea gas transfer: Its dependence on wind stress, small-scale roughness, and surface films, *J. Geophys. Res.*, *109*, C08S17, doi:10.1029/2003JC002131.

Gålfalk, M., D. Bastviken, S. Fredriksson, and L. Arneborg (2013), Determination of the piston velocity for water-air interfaces using flux chambers, acoustic Doppler velocimetry, and IR imaging of the water surface, *J. Geophys. Res. Biogeosci.*, *118*, 770–782, doi:10.1002/jgrg.20064.

Handler, R. A., and Q. Zhang (2013), Direct numerical simulations of a sheared interface at low wind speeds with applications to infrared remote sensing, *IEEE J.-Stars*, *6*(3), 1086–1091, doi:10.1109/Jstars.2013.2241736.

Handler, R. A., R. I. Leighton, G. B. Smith, and R. Nagaosa (2003), Surfactant effects on passive scalar transport in a fully developed turbulent flow, *Int. J. Heat Mass Transfer*, *46*(12), 2219–2238, doi:10.1016/S0017-9310(02)00526-4.

Hasegawa, Y., and N. Kasagi (2008), Systematic analysis of high Schmidt number turbulent mass transfer across clean, contaminated and solid interfaces, *Int. J. Heat Fluid Flow*, *29*(3), 765–773, doi:10.1016/j.ijheatfluidflow.2008.03.002.

Herlina, H., and J. G. Wissink (2014), Direct numerical simulation of turbulent scalar transport across a flat surface, *J. Fluid Mech.*, *744*, 217–249, doi:10.1017/Jfm.2014.68.

Jahne, B., and H. Haussecker (1998), Air-water gas exchange, *Annu. Rev. Fluid Mech.*, *30*, 443–468

Jahne, B., K. O. Munnich, R. Bosinger, A. Dutzi, W. Huber, and P. Libner (1987), On the parameters influencing air-water gas-exchange, *J. Geophys. Res.*, *92*(C2), 1937–1949.

Jahne, B., P. Libner, R. Fischer, T. Billen, and E. J. Plate (1989), Investigating the transfer processes across the free aqueous viscous boundary layer by the controlled flux method, *Tellus, Ser. B*, *41*(2), 177–195, doi:10.1111/j.1600-0889.1989.tb00135.x.

Jeffery, C. D., D. K. Woolf, I. S. Robinson, and C. J. Donlon (2007), One-dimensional modelling of convective CO_2 exchange in the Tropical Atlantic, *Ocean Modell.*, *19*(3-4), 161–182, doi:10.1016/j.ocemod.2007.07.003.

Jessup, A. T., W. E. Asher, M. Atmane, K. Phadnis, C. J. Zappa, and M. R. Loewen (2009), Evidence for complete and partial surface renewal at an air-water interface, *Geophys. Res. Lett.*, *36*, L16601, doi:10.1029/2009GL038986.

Jonsson, A., J. Aberg, A. Lindroth, and M. Jansson (2008), Gas transfer rate and CO(2) flux between an unproductive lake and the atmosphere in northern Sweden, *J. Geophys. Res.*, *113*, G04006, doi:10.1029/2008JG000688.
Kou, J., K. P. Judd, and J. R. Saylor (2011), The temperature statistics of a surfactant-covered air/water interface during mixed convection heat transfer and evaporation, *Int. J. Heat Mass Transfer*, *54*(15-16), 3394–3405, doi:10.1016/j.ijheatmasstransfer.2011.03.047.
Kubrak, B., H. Herlina, F. Greve, and J. G. Wissink (2013), Low-diffusivity scalar transport using a WENO scheme and dual meshing, *J. Comput. Phys.*, *240*, 158–173, doi:10.1016/j.jcp.2012.12.039.
Kundu, P. K., I. M. Cohen, and D. R. Dowling (2012), *Fluid Mechanics*, 5th ed., pp. 1–891, Academic Press, Elsevier, Waltham, Mass.
Lamont, J. C. (1960), *Gas Absorption in Cocurrent Turbulent Bubble Flow*, Univ. of B. C., Vancouver, Canada.
Lamont, J. C., and D. S. Scott (1970), An eddy cell model of mass transfer into surface of a turbulent liquid, *AIChE J.*, *16*(4), 513.
Ledwell, J. J. (1984), The variation of the gas transfer coefficient with molecular diffusivity, in *Gas Transfer at Water Surfaces*, edited by B. W. Brutsaert and G. H. Jirka, pp. 293–302, Springer, Dordrecht, Netherlands, doi:10.1007/978-94-017-1660-4_27.
Leighton, R. I., G. B. Smith, and R. A. Handler (2003), Direct numerical simulations of free convection beneath an air-water interface at low Rayleigh numbers, *Phys. Fluids*, *15*(10), 3181–3193, doi:10.1063/1.1606679.
Macintyre, S., W. Eugster, and G. W. Kling (2002), The critical importance of buoyancy flux for gas flux across the air-water interface, in *Gas Transfer at Water Surfaces*, edited by M. A. Donelan et al., pp. 135–139, AGU, Washington, D. C., doi:10.1029/GM127p0135.
Magnaudet, J., and I. Calmet (2006), Turbulent mass transfer through a flat shear-free surface, *J. Fluid Mech.*, *553*, 155–185, doi:10.1017/S0022112006008913.
Mccready, M. J., E. Vassiliadou, and T. J. Hanratty (1986), Computer-simulation of turbulent mass-transfer at a mobile interface, *AIChE J.*, *32*(7), 1108–1115, doi:10.1002/aic.690320707.
McKenna, S. P., and W. R. McGillis (2004), The role of free-surface turbulence and surfactants in air-water gas transfer, *Int. J. Heat Mass Transfer*, *47*(3), 539–553, doi:10.1016/j.ijheatmasstransfer.2003.06.001.
Na, Y., D. V. Papavassiliou, and T. J. Hanratty (1999), Use of direct numerical simulation to study the effect of Prandtl number on temperature fields, *Int. J. Heat Fluid Flow*, *20*(3), 187–195, doi:10.1016/S0142-727x(99)00008-9.
Nagaosa, R., and R. A. Handler (2012), Characteristic time scales for predicting the scalar flux at a free surface in turbulent open-channel flows, *AIChE J.*, *58*(12), 3867–3877, doi:10.1002/aic.13773.
Nagaosa, R. S. (2014), Reprint of: A numerical modelling of gas exchange mechanisms between air and turbulent water with an aquarium chemical reaction, *J. Comput. Phys.*, *271*, 172–190, doi:10.1016/j.jcp.2014.04.007.
Papavassiliou, D. V., and T. J. Hanratty (1997), Transport of a passive scalar in a turbulent channel flow, *Int. J. Heat Mass Transfer*, *40*(6), 1303–1311, doi:10.1016/S0017-9310(96)00202-5.
Pierce, D. W., T. P. Barnett, K. M. AchutaRao, P. J. Gleckler, J. M. Gregory, and W. M. Washington (2006), Anthropogenic warming of the oceans: Observations and model results, *J. Clim.*, *19*(10), 1873–1900, doi:10.1175/JCLI3723.1.
Prasad, A. K., and P. V. Gonuguntla (1996), Turbulence measurements in nonpenetrative thermal convection, *Phys. Fluids*, *8*(9), 2460–2470, doi:10.1063/1.869031.
Read, J. S., et al. (2012), Lake-size dependency of wind shear and convection as controls on gas exchange, *Geophys. Res. Lett.*, *39*, L09405, doi:10.1029/2012GL051886.
Rutgersson, A., A. Smedman, and E. Sahlee (2011), Oceanic convective mixing and the impact on air-sea gas transfer velocity, *Geophys. Res. Lett.*, *38*, L02602, doi:10.1029/2010GL045581.
Soloviev, A. X., and P. Schlussel (1994), Parameterization of the cool skin of the ocean and of the air ocean gas transfer on the basis of modeling surface renewal, *J. Phys. Oceanogr.*, *24*(6), 1339–1346
Townsend, A. A. (1959), Temperature fluctuations over a heated horizontal surface, *J. Fluid Mech.*, *5*(2), 209–241, doi:10.1017/S0022112059000167.
Tranvik, L. J., et al. (2009), Lakes and reservoirs as regulators of carbon cycling and climate, *Limnol. Oceanogr. Methods*, *54*(6), 2298–2314, doi:10.4319/lo.2009.54.6_part_2.2298.
Turney, D. E., W. C. Smith, and S. Banerjee (2005), A measure of near-surface fluid motions that predicts air-water gas transfer in a wide range of conditions, *Geophys. Res. Lett.*, *32*, L04607, doi:10.1029/2004GL021671.
Veron, F., W. K. Melville, and L. Lenain (2008), Infrared techniques for measuring ocean surface processes, *J. Atmos. Oceanic Technol.*, *25*(2), 307–326, doi:10.1175/2007jtech0524.1.
Versteeg, H. K., and W. Malalasekera (2007), *An Introduction to Computational Fluid Dynamics: The Finite Volume Method*, 2nd ed., xii, 503 p., Pearson Educ. Ltd., Harlow, U. K.
Vesala, T., J. Huotari, U. Rannik, T. Suni, S. Smolander, A. Sogachev, S. Launiainen, and A. Ojala (2006), Eddy covariance measurements of carbon exchange and latent and sensible heat fluxes over a boreal lake for a full open-water period, *J. Geophys. Res.*, *111*, D11101, doi:10.1029/2005JD006365.
Volino, R. J., and G. B. Smith (1999), Use of simultaneous IR temperature measurements and DPIV to investigate thermal plumes in a thick layer cooled from above, *Exp. Fluids*, *27*(1), 70–78.
Wanninkhof, R., W. E. Asher, D. T. Ho, C. Sweeney, and W. R. McGillis (2009), Advances in quantifying air-sea gas exchange and environmental forcing, *Annu. Rev. Mar. Sci.*, *1*, 213–244, doi:10.1146/annurev.marine.010908.163742.
Yu, L. S., and R. A. Weller (2007), Objectively analyzed air-sea heat fluxes for the global ice-free oceans (1981-2005), *Bull. Am. Meteorol. Soc.*, *88*(4), 527, doi:10.1175/BAMS-88-4-527.
Zappa, C. J., P. A. Raymond, E. A. Terray, and W. R. McGillis (2003), Variation in surface turbulence and the gas transfer velocity over a tidal cycle in a macro-tidal estuary, *Estuaries*, *26*(6), 1401–1415, doi:10.1007/BF02803649.
Zappa, C. J., W. E. Asher, A. T. Jessup, J. Klinke, and S. R. Long (2004), Microbreaking and the enhancement of air-water transfer velocity, *J. Geophys. Res.*, *109*, C08S16, doi:10.1029/2003JC001897.
Zappa, C. J., W. R. McGillis, P. A. Raymond, J. B. Edson, E. J. Hintsa, H. J. Zemmelink, J. W. H. Dacey, and D. T. Ho (2007), Environmental turbulent mixing controls on air-water gas exchange in marine and aquatic systems, *Geophys. Res. Lett.*, *34*, L10601, doi:10.1029/2006GL028790.
Zhang, Q., R. A. Handler, and S. T. Fredriksson (2013), Direct numerical simulation of turbulent free convection in the presence of a surfactant, *Int. J. Heat Mass Transfer*, *61*, 82–93, doi:10.1016/j.ijheatmasstransfer.2013.01.031.

Erratum

In the originally published version of this article,an incorrect version of Equation 32 was published. This has been corrected, and this version may be considered the authoritative version of record.